Available online at www.sciencedirect.com
ScienceDirect
Journal of the Mechanics and Physics of Solids 56 (2008) 2642–2668
JOURNAL OF THE MECHANICS AND PHYSICS OF SOLIDS
www.elsevier.com/locate/jmps

Mechanics of deformation-triggered pattern transformations and superelastic behavior in periodic elastomeric structures

K. Bertoldi[a,*], M.C. Boyce[a], S. Deschanel[a], S.M. Prange[a], T. Mullin[b]

[a]*Department of Mechanical Engineering, Massachusetts Institute of Technology, Cambridge, MA 02139-4307, USA*
[b]*Manchester Centre for Nonlinear Dynamics, The University of Manchester, Manchester M13 9PL, UK*

Received 6 September 2007; received in revised form 3 March 2008; accepted 7 March 2008

Abstract

Recently, novel and uniform deformation-induced pattern transformations have been found in periodic elastomeric cellular solids upon reaching a critical value of applied load [Mullin, T., Deschanel, S., Bertoldi, K., Boyce, M.C., 2007. Pattern transformation triggered by deformation. Phys. Rev. Lett. 99, 084301; Boyce, M.C., Prange, S.M., Bertoldi, K., Deschanel, S., Mullin, T., 2008. Mechanics of periodic elastomeric structures. In: Boukamel, Laiarinandrasana, Meo, Verron (Eds.), Constitutive Models for Rubber, vol. V. Taylor & Francis Group, London, pp. 3–7]. Here, the mechanics of the deformation behavior of several periodically patterned two-dimensional elastomeric sheets are investigated experimentally and through numerical simulation. Square and oblique lattices of circular voids and rectangular lattices of elliptical voids are studied. The numerical results clearly show the mechanism of the pattern switch for each microstructure to be a form of local elastic instability, giving reversible and repeatable transformation events as confirmed by experiments. Post-deformation transformation is observed to accentuate the new pattern and is found to be elastic and to occur at nearly constant stress, resulting in a superelastic behavior. The deformation-induced transformations have been physically realized on structures constructed at the millimeter length scale. This behavior should also persist at the micro and nano length scales, providing opportunities for transformative photonic and phononic crystals which can switch in a controlled manner and also exploiting the phenomenon to imprint complex patterns.

Keywords: Elastomers; Periodic structures; Microscopic instability; Macroscopic instability

1. Introduction

There are many examples of cellular solids in nature and they are mimicked in numerous synthetic materials ranging from heterogeneous foams to engineered honeycombs. These cellular structures are used in a wide variety of mechanical, acoustic and thermal applications. The connections between the microstructure of such materials and their macroscopic properties have been investigated by many researchers as summarized in the book by Gibson and Ashby (1997). Research into the mechanics and structural properties of cellular solids may be categorized according to the designed role of the material: high stiffness to weight; high strength to

*Corresponding author.
E-mail address: bertoldk@mit.edu (K. Bertoldi).

0022-5096/$ - see front matter © 2008 Elsevier Ltd. All rights reserved.
doi:10.1016/j.jmps.2008.03.006

weight; or low density, high energy absorption materials. Energy absorption is achieved by capitalizing on the large deformations and collapse of the cellular structures when deformed beyond the initial linear elastic regime. The nonlinear stress–strain behavior of foams which possess a heterogeneous cell structure and honeycombs which possess a periodic structure have been of particular interest. Under compression, the transition from linear elastic behavior to either a ''yield'' or plateau stress (or, in some instances, a ''yield'' with some subsequent strain hardening) has been found to result from an initial instability. This usually originates in the buckling of a member or a wall in the cell microstructure which then leads to localized deformation into bands. The collapse bands can progress through the structure at relatively constant stress. This energy absorbing, collapse behavior has been clearly demonstrated in experimental and modeling studies of a wide range of two-dimensional honeycomb structures including hexagonal (e.g., Papka and Kyriakides, 1994, 1998a; Triantafyllidis and Schraad, 1998; Ohno et al., 2002) and circular (e.g., Papka and Kyriakides, 1998b, 1999a, b; Tantikom et al., 2005a, b) structures with different wall dimensions and elastic–plastic mechanical behavior. The two-dimensional periodic honeycomb structures have enabled investigators to vary different parameters in a controlled manner to study the effect of geometric features and imperfections on the onset of the instability and its subsequent localization into deformation bands.

The focus of this paper is on the mechanics of deformation of two-dimensional periodic elastomeric cellular structures. As discussed above, cellular structures provide unique energy absorption opportunities through their nonlinear stress–strain behavior—particularly through the ability to undergo very large deformation at constant or near constant stress once localization takes place. While this mechanical function of cellular solids is of great importance, it should also be recognized that periodic structures also provide many other functions and/or attributes in natural materials. Studies on butterflies, beetles, moths, birds and fish (Ghiradella, 1994; Parker et al., 2001; Vukusic and Sambles, 2003; Prum et al., 2006; Kemp et al., 2006) have shown that the iridescent phenomena are related to the presence of surface and/or subsurface photonic crystal microstructures. Photonic crystals are composed of submicron structures with periodicity comparable to the wavelength of visible light which are designed to affect the propagation of electromagnetic waves. Therefore, they are attractive optical materials for controlling and manipulating light with applications including LEDs, optical fibers, nanoscopic lasers, ultrawhite pigment, radio frequency antennas and reflectors, and photonic integrated circuits. In a similar way, phononic crystals are periodic composite materials with lattice spacings comparable to the acoustic wavelength (e.g., Yang et al., 2004). They are of interest because of the profound effects of their periodic structure on wave propagation (e.g., the existence of acoustic band gaps), and because of potential applications as sound filters, transducer design and acoustic mirrors (Kushwaha et al., 1993; Kafesaki et al., 1995). Periodic submicron structures are also employed to obtain super-hydrophobicity. Microtextures that modify the wettability of the material have been found in the leaves of about 200 plants, including asphodelus, drosera, eucalyptus, euphorbia, gingko biloba, iris, lotus, and tulipa (Barthlott and Neinhuis, 1997; Neinhuis and Barthlott, 1997), as well as in butterfly wings, duck feathers, bugs and desert beetles (Lee et al., 2004; Wagner et al., 1996; Parker and Lawrence, 2001).

Recently, the ability to synthetically produce periodic structures at the micron and submicron length scales through microfabrication processes (Kinoshita and Yoshioka, 2005; Campbell et al., 2000), interference lithography (Hennessy et al., 2003; Thylen et al., 2004; Ullal et al., 2004; Cheng et al., 2004; Choi et al., 2006; Jang et al., 2006), as well as thermodynamically driven self-assembly (Zhai et al., 2006; Shevchenko et al., 2006) has created new opportunities to mimic natural structures and properties. These periodic structures are generally static or, in some instances, change in a more or less affine nature with deformation or other external stimuli (Park and Lee, 2004; Aschwanden and Stemmer, 2006). Hence, properties which are dependent on the precise length scale and/or spacing of the periodic features will exhibit a gradual monotonic change with deformation.

Here, we investigate the ability to use deformation to trigger dramatic homogeneous pattern transformations in certain classes of simple periodic elastomeric structures. The transformations are triggered at relatively low strains and are found to be a result of an elastic instability, and are thus reversible and repeatable. Interestingly, the pattern transformations are found to be homogeneous in the sense that they do not lead to localized deformation bands, but occur throughout the structure. This enables new opportunities to utilize this mechanical deformation behavior to control attributes that depend on the periodic pattern (Bertoldi and Boyce, 2008). Below, we present the results of experiments and models that reveal the mechanics

of several periodically patterned two-dimensional elastomeric sheets during axial compression. Although experimental results are presented for structures fabricated at the millimeter length scale, the deformation-induced transformations are equally applicable to analogous periodic microstructures produced at the micron and nano-scales and thus enable several avenues for new materials with transformative photonic, phononic and hydrophobic/hydrophilic attributes.

2. Experiments

2.1. Experimental protocol

Specimens with a range in periodic lattice microstructures were water jet cut from sheets of the photoelastic elastomer PSM-4 (Zuriguel et al., 2007). Five finite-sized periodic structures (see Fig. 1, first row) have been tested:

- *Specimen 1*: 101 mm × 101 mm and 9.4 mm thick, comprising a microstructure of a 10 × 10 square array of circular holes of 8.67 mm diameter with 9.97 mm center-to-center spacing, vertically and horizontally, and 5.64 mm from the center of the lateral holes to the edge of the specimen.
- *Specimen 2*: 112 mm × 112 mm and 9.4 mm thick, comprising a microstructure of a 10 × 10 square array of circular holes of 8.67 mm diameter with 10.97 mm center-to-center spacing, vertically and horizontally, and 6.64 mm from the center of the lateral holes to the edge of the specimen.
- *Specimen 3*: 133.2 mm × 102.5 mm and 6.9 mm thick, comprising a microstructure of a 12 × 17 rectangular array of elliptical holes of 5.01 mm and 2.67 mm semi-axes with center-to-center spacing of 5.99 mm vertically and 11.02 mm horizontally; the distance between the center of the elliptical voids of top (bottom) row and the top (bottom) edge is 3.32 mm, whereas the distance between the center of the elliptical voids closest to the lateral edges and the lateral edges is 6.01 mm.
- *Specimen 4*: 104 mm × 98.5 mm and 9.4 mm thick, comprising a microstructure of a 9.5 × 10 oblique array of circular holes of 8.67 mm diameter with center-to-center spacing of 9.47 mm vertically and 10.97 mm

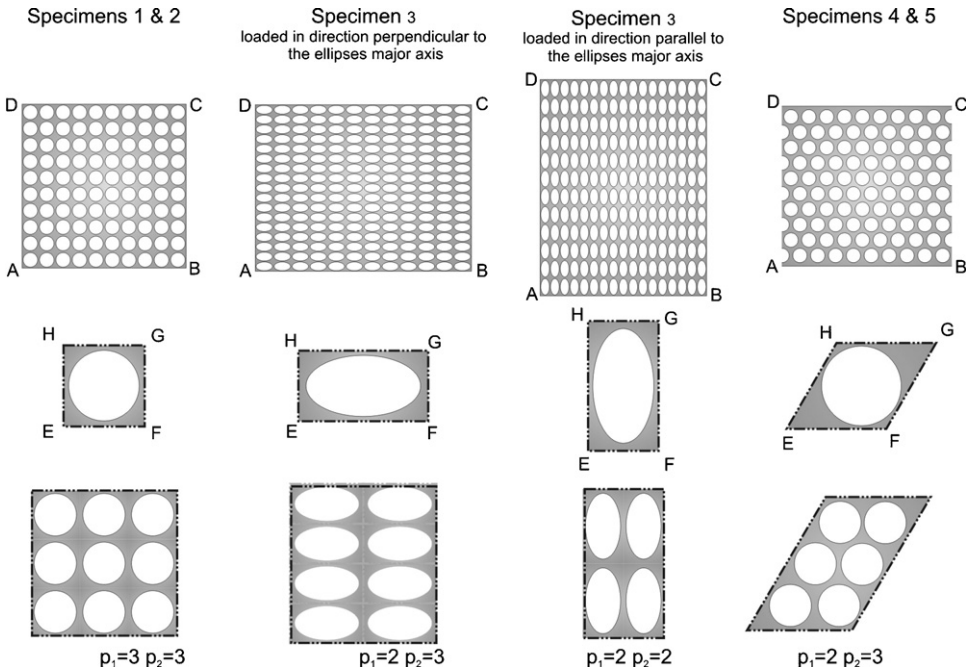

Fig. 1. Full specimens (top row), corresponding primitive cells (center row) and corresponding $p_1 \times p_2$ periodic representative volume elements (bottom row); Specimens 1 and 2 differ by ligament thickness, whereas Specimens 4 and 5 differ by both horizontal and vertical center-to-center spacing.

horizontally; the distance between the center of the circular voids of top (bottom) row and the top (bottom) edge is 6.64 mm.

- *Specimen 5*: 114 mm × 109 mm and 9.4 mm thick, comprising a microstructure of a 9.5 × 10 oblique array of circular holes of 8.67 mm diameter with center-to-center spacing of 10.42 mm vertically and 11.97 mm horizontally; the distance between the center of the circular voids of top (bottom) row and the top (bottom) edge is 7.64 mm.

Each specimen was subjected to uniaxial compression in the plane of the sheet at a constant nominal strain rate of $10^{-4}\,s^{-1}$ using a Zwick screw-driven testing machine. Specimen 3 was tested by applying uniaxial compression in directions parallel and perpendicular to the major axis of the elliptical holes in separate experiments. All specimens were placed between two close fitting 5-mm-thick polymethylmethacrylate (PMMA) sheets to eliminate out-of-plane buckling. Chalk was lightly dusted on the surfaces to help reduce frictional effects. The specimen and PMMA sheets were located on the Zwick platen and an aluminum bar spanning the entire cross-section of the specimen was used to uniformly displace the top surface. A photo-flood lamp back-lit the apparatus and both still and video images were recorded. The nominal stress vs. nominal strain behavior was recorded automatically as computed from the measured force and displacement.

2.2. Experimental results

2.2.1. Circular holes on a square lattice

Experimental results for the nominal stress vs. nominal strain behavior up to a compressive strain of 0.10 are shown in Fig. 2 (left) for the two square arrays of circular holes (Specimens 1 and 2) which are characterized by different center-to-center spacing. The square arrays exhibit an initial linear elastic behavior with a sudden departure from linearity to a plateau stress. The departure from linearity is a result of a sudden transformation in the periodic pattern as shown in the snapshots of deformed configurations at different strains (Fig. 2 (right)).

During loading in the experiment, the instability is somewhat abrupt and characterized by a drop in nominal stress as seen in Fig. 2; subsequent experimental loading cycles (not shown) retrace this loading curve. The unloading exhibits a small amount of hysteresis which may result from the combination of a very small level of viscoelasticity in this elastomer (the material stress–strain behavior will be presented in Section 3.1) and a small amount of friction between the PMMA plates and the specimen. This elastic loading–unloading behavior where the stress increases in a nearly linear manner to a stress plateau and undergoes reversible,

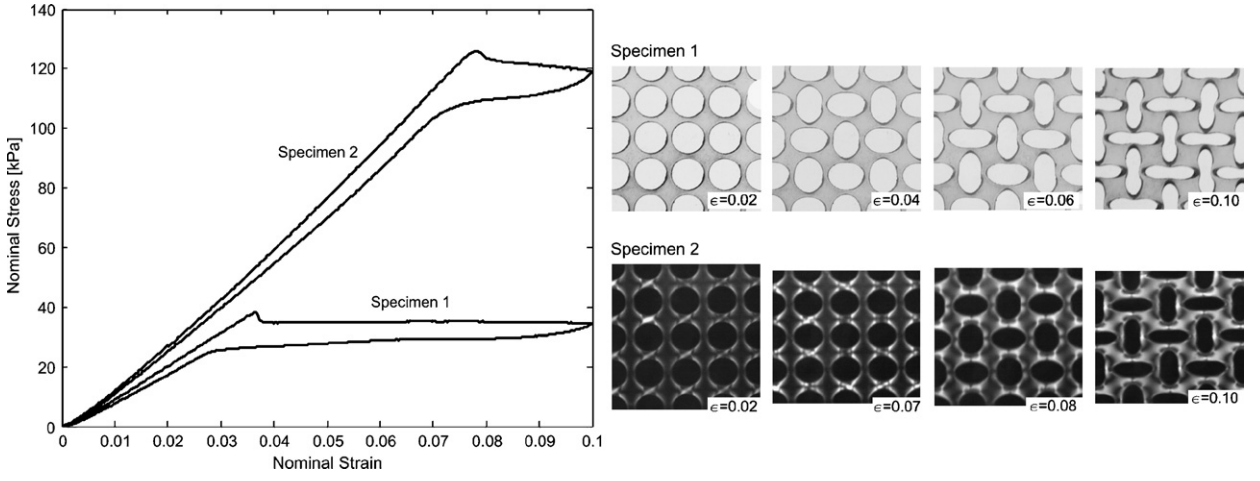

Fig. 2. Experimental nominal stress vs. nominal strain curves (left) for Specimens 1 and 2 (square arrays of 8.67 mm diameter circular holes with 9.97 and 10.97 mm center-to-center spacing, respectively). On the right, experimental images of Specimen 1 (top) at macroscopic strain of 2%, 4%, 6%, and 10% and of Specimen 2 (bottom) at macroscopic strain of 2%, 7%, 8%, and 10%. The departures from linearity are the result of elastic instabilities in the microstructures that trigger the observed pattern transformations.

repeatable large deformation at near constant stress is characteristic of superelastic behavior. The critical triggering stress level of Specimen 2 is observed to be approximately a factor of 3 higher than that of Specimen 1, scaling by the ratio of the $(t/R)^2$ of the two cases (here t is the ligament thickness and R is the hole diameter). This scaling is consistent with ligament buckling governing the initiation of the stress plateau.

The experimental images of the deformed configurations are shown in Fig. 2 (right) for Specimens 1 (top) and 2 (bottom). During the linear elastic range of deformation, the circular holes are observed to undergo a gradual and homogeneous compression. This relatively affine-like deformation is replaced by a transformation to a pattern of alternating, mutually orthogonal ellipses above a nominal strain of 0.04 (nominal stress of 37 kPa) for Specimen 1, and 0.07 (120 kPa) for Specimen 2. This pattern transformation corresponds to the plateau region immediately after the departure from linearity. Once formed, the new pattern becomes further accentuated in shape such that the major axis of each ellipse lengthens while its minor axis shortens with increasing macroscopic compressive strain. This can be seen in the deformed configurations of Fig. 2 for Specimen 1 (top) at strains of 0.06 and 0.10 and for Specimen 2 (bottom) at a strain of 0.10. After transformation to the new configuration, much of the macroscopic deformation is observed to be accommodated by the ongoing accentuation of the ellipses which results in a simple rotation of the four main matrix domains diagonally bridging neighboring holes. These domains experience negligible strain but undergo large rotations. This local behavior has also been observed to be a deformation mechanism in thermoplastic vulcanizates (Boyce et al., 2001).

2.2.2. *Elliptical holes on a rectangular lattice*

The results obtained for the square array of circular holes encourages pursuit of other such periodic elastomeric structures. Here, a rectangular array of elliptical holes (Specimen 3) has been tested in uniaxial compression in directions parallel and perpendicular to the major axis of the constituent elliptical holes. The nominal stress–strain behaviors for both directions of compression are shown in Fig. 3 (left), with corresponding deformation images shown in Fig. 3 (right).

The stress–strain behavior is observed to be linear elastic with homogeneous compression up to a strain of 0.03 for compression perpendicular to the major axis and up to a strain of 0.015 for compression parallel to the major axis. The stress then plateaus as a result of the pattern transformation event. Again, the transformation is a result of a local elastic buckling instability in the ligaments, giving reversible and repeatable pattern transformations. In both of these cases, the array of identical ellipses are observed to transform to alternating arrays of high and low aspect ratio ellipses where the aspect ratio contrast increases with increasing macroscopic strain and the low aspect ratio ellipses become nearly circular. It is interesting to note that the final pattern which emerges is independent of the direction of the applied strain and that the ratio of the critical strain required for the pattern transformation is approximately proportional to that of the major to minor axes.

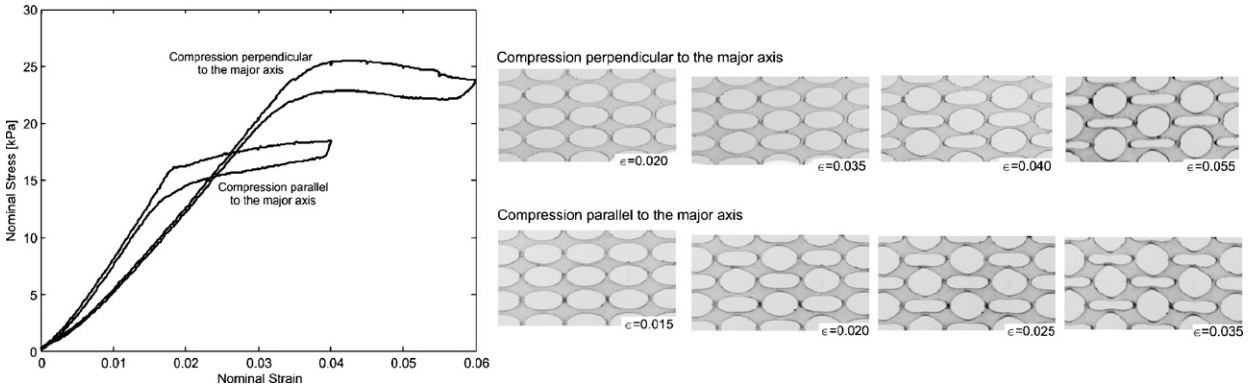

Fig. 3. Experimental nominal stress vs. nominal strain curves for Specimen 3 (rectangular array of elliptical holes) compressed in a direction perpendicular to the major axis and parallel to the major axis (left). On the right, experimental images of the specimen compressed in a direction perpendicular to the major axis (top) at macroscopic strains of 2%, 3.5%, 4%, and 5.5% and compressed in a direction parallel to the major axis (bottom) at strains of 1.5%, 2%, 2.5%, and 3.5%.

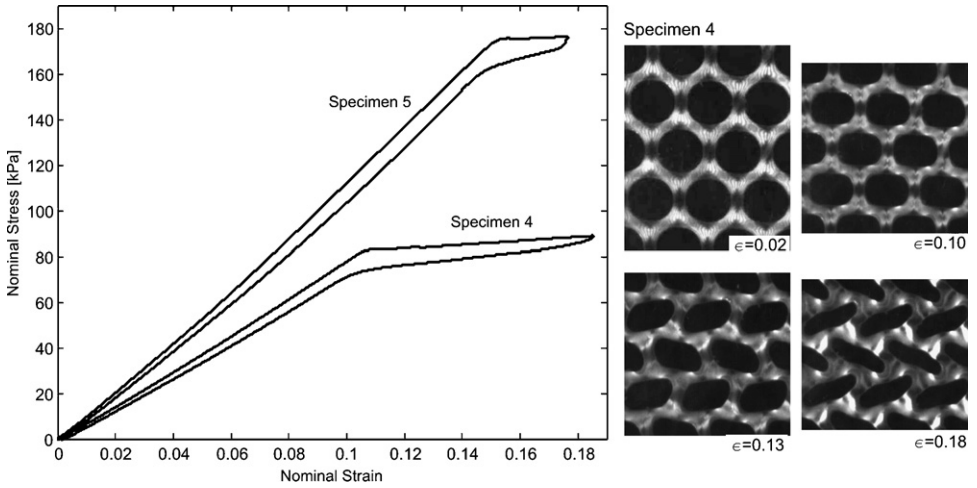

Fig. 4. Nominal stress vs. nominal strain curves for Specimens 4 and 5 (oblique arrays of circular holes) showing experimental results (left). On the right, experimental images at macroscopic strain of 2%, 10%, 13%, and 18% for Specimen 4.

2.2.3. *Circular holes on an oblique lattice*

Here, the compression results of two oblique arrays of circular voids (Specimens 4 and 5) with the same diameter but with different center-to-center spacing (both horizontally and vertically) are presented. The nominal stress–strain behaviors for both specimens up to a compressive strain of 0.18 are shown in Fig. 4 (left) with corresponding deformation images for Specimen 4 shown in Fig. 4 (right). The material behavior is characterized by an initial linear response followed by a load plateau starting at a strain of 0.11 for Specimen 4 and at a strain of 0.15 for Specimen 5. Initially, the oblique array is observed to be linearly elastic with homogeneous and gradual compression of the circular holes (see images of the deformed configuration at strains of 0.02, 0.10 for Specimen 4 in Fig. 4 (right)); at this stage the deformation is accommodated by local shearing of the diagonal matrix domains, a mechanism that has also been found in thermoplastic vulcanizates (Boyce et al., 2001).

The oblique array is observed to provide a more compliant initial elastic behavior than that observed in the square array as found by comparing cases with nearly identical area fractions of voids. The stiffer behavior of the square array is due to the presence of continuous vertical ligaments coaxial with the compression axis; these vertical ligaments are directly axially loaded and provide the enhanced initial axial stiffness. The absence of axially compressed vertical ligaments in the oblique array not only provides a more compliant structure, but also delays the destabilizing buckling trigger that initiates the transformation observed in the square array. The pattern transformation in the oblique array is a result of a critical intervoid shear instability event. Hence, the pattern after transformation is one of sheared voids where the shear direction alternates back and forth from row to row.

3. Modeling

Numerical simulations of the deformation of the five finite-sized periodic specimens described in Section 2 were conducted utilizing the nonlinear finite element code ABAQUS. Each mesh was constructed of six-node, quadratic, hybrid, plane strain elements (ABAQUS element type CPE6 H).[1] The accuracy of each mesh was ascertained through a mesh refinement study. The experimental results presented in Section 2 suggest that the pattern transformation is a result of a local buckling instability in the compressively loaded vertical inter-hole ligaments in the case of the square arrays and is a result of a shear instability in the diagonally bridging

[1]This particular hybrid element independently interpolates the pressure in order to address the near incompressibility of this constitutive behavior (Hibitt et al., 2006).

ligaments in the case of the oblique arrays. These instabilities trigger the change to the new configuration. Hence, instability analyses are conducted on all finite-sized specimens. The stress–strain behavior subsequent to the instability-triggered transformation is simulated utilizing information from the instability analysis to perturb the mesh and capture post-instability deformation behavior of the periodic structures.

Recognizing that the finite-sized specimens are necessarily influenced by boundary conditions at both the loaded and the traction free edges (due to a boundary layer of matrix material), the deformation behavior of infinite periodic arrays are also modeled. For the case of an infinite periodic solid Geymonat et al. (1993) showed that the eigenmodes of microscopic bifurcation can have a longer periodic length than a "unit cell". A unit cell is identified here as the smallest repeating geometric unit, also referred to as the "primitive cell" in classical physics (e.g., Kittel, 1986). In the limiting case of a periodic length of infinity, the microscopic bifurcation can be identified with the start of macroscopic instability. Therefore, when a macroscopic deformation is imposed on a periodic solid with a primitive cell Y (Fig. 1 (center)), its microscopic deformation initially satisfies the so-called Y-periodicity, in which Y is the unit of periodicity. However, when bifurcation occurs, the Y-periodicity may break down, resulting in a periodic unit larger than Y, so that an enlarged cell aggregate $\mathbf{p}Y$ consisting of $\mathbf{p} = (p_1, p_2)$ unit cells, needs to be considered (Muller, 1987). Following these findings, different approaches have been developed to investigate the bifurcations occurring in infinite periodic solids. Bloch wave analysis, a staple of physics long used to examine electronic, photonic and phononic band structures in periodic lattices, has been utilized to predict the microstructural deformation instability mode in periodic structures by applying a Bloch wave perturbation to the unit cell (Triantafyllidis and Schnaidt, 1993; Triantafyllidis and Schraad, 1998; Triantafyllidis et al., 2006). Alternatively, Saiki et al. (2002) employed the block-diagonalization method to determine the size of the RVE that can accommodate the most critical bifurcation mode. Ohno et al. (2002) and Okumura et al. (2004) used a two-scale theory of the updated Lagrangian type to analyze the microscopic bifurcation and post-bifurcation behavior of elastoplastic, periodic cellular solids. Laroussi et al. (2002) obtained the failure surface for open cell-foams through two methods: the first one consists of traditional eigenvalue instability analyses on representative volume elements (RVEs) of increasing size (each with general periodic boundary conditions) and the second method considers both periodic and non-periodic displacements variation on a minimum unit cell. Below we present two approaches to investigate the onset of microscopic instabilities in infinite periodic solids. The first method follows that of Laroussi et al. (2002) considering eigenmode analyses on representative volume elements of increasing size (increasing number of repeating units in the RVEs) and will be referred to as Refined Eigen Analysis. The second approach (referred to as Bloch wave analysis) follows the approach utilized in Triantafyllidis et al. (2006), where the instability modes of the infinite periodic solid are examined performing Bloch wave calculations on the primitive cell.

Therefore, after characterization of the material response through uniaxial compression stress–strain tests (Section 3.1) and discretization of the structure for finite element analysis, analyses of the behavior of both the finite-sized specimens and the infinite periodic arrays involve the following four steps:

- definition of appropriate boundary conditions (Section 3.2);
- instability analysis (Section 3.3);
- introduction of an imperfection into the mesh (Section 3.4);
- load–displacement analysis capturing the initial (nearly) linear behavior, the critical transformation event and the post-transformation behavior (Section 3.4).

3.1. Material behavior

Uniaxial compression stress–strain tests were conducted to characterize the material response of the elastomeric matrix. The specimens were subjected to uniaxial compression at a constant nominal strain rate of 0.05 and $0.005\,s^{-1}$ using a Zwick screw-driven testing machine. The tests show that the material exhibits a behavior typical for elastomers: large strain elastic behavior with negligible rate dependence and negligible hysteresis during a loading–unloading cycle. The material behavior at a strain rate of $0.05\,s^{-1}$ is reported in Fig. 1.

The observed constitutive behavior is modeled as hyperelastic. Let $\mathbf{F}=\partial\mathbf{x}/\partial\mathbf{X}$ be the deformation gradient, mapping a material point from the reference position $\mathbf{X}$ to its current location $\mathbf{x}$ and J be its determinant, $J=\det\mathbf{F}$. For an isotropic hyperelastic material the strain energy density W can be expressed as a function of the invariants of the right Cauchy-Green tensor $\mathbf{C}=\mathbf{F}^{\mathrm{T}}\mathbf{F}$ (or, alternatively, also the left Cauchy-Green tensor $\mathbf{B}=\mathbf{F}\mathbf{F}^{\mathrm{T}}$),

$$W=W(I_1,I_2,I_3), \tag{1}$$

where

$$I_1=\operatorname{tr}\mathbf{C},\quad I_2=\tfrac{1}{2}[(\operatorname{tr}\mathbf{C})^2-\operatorname{tr}\mathbf{C}^2],\quad I_3=\det\mathbf{C}=J^2, \tag{2}$$

I_1 being essentially a scalar equivalent stretch measure and I_3 the square of the volume ratio. Here, the PSM-4 stress–strain behavior is modeled using a two-term I_1-based Rivlin model (Rivlin and Saunders, 1951) modified to include compressibility (with a high bulk modulus):

$$W(I_1,I_3)=c_1(I_1-3)+c_2(I_1-3)^2-2c_1\log J+\frac{K}{2}(J-1)^2, \tag{3}$$

where c_1 and c_2 are material constants and K is the bulk modulus. For the particular case of $c_2=0$, Eq. (3) reduces to a compressible version of the neo-Hookean model. The Cauchy stress, is given by

$$\boldsymbol{\sigma}=\frac{2}{J}\frac{\partial W}{\partial I_1}\mathbf{B}+\frac{\partial W}{\partial J}\mathbf{I}, \tag{4}$$

yielding

$$\boldsymbol{\sigma}=\frac{2}{J}[c_1+2c_2(I_1-3)]\mathbf{B}+\left[K(J-1)-2\frac{c_1}{J}\right]\mathbf{I}, \tag{5}$$

with corresponding first Piola–Kirchoff stress $\mathbf{S}$ found as

$$\mathbf{S}=J\boldsymbol{\sigma}\mathbf{F}^{-\mathrm{T}}=2[c_1+2c_2(I_1-3)]\mathbf{F}+J\left[K(J-1)-2\frac{c_1}{J}\right]\mathbf{F}^{-\mathrm{T}}. \tag{6}$$

The material was modeled as nearly incompressible, characterized by $K/\mu=50$, where μ denotes the initial shear modulus. From the compression data shown in Fig. 5, the initial Young's modulus was measured to be 3.25 MPa, so that $c_1=\mu/2=0.55$ MPa. Fig. 5 shows that the neo-Hookean model captures the behavior very well up to a strain of about 0.1 which covers the majority of the strain levels studied, whereas the addition of the second I_1-based term with $c_2=0.3$ MPa gives the two-term Rivlin model which captures the behavior up to a strain of about 0.40.

3.2. Boundary conditions

3.2.1. Finite-sized periodic specimens

To simulate the experimental tests for the finite-sized periodic specimen (Fig. 1 (top)), the bottom edge AB is fixed in the vertical direction (node A is also fixed in the horizontal direction to prevent a rigid body motion), whereas the top edge CD is uniformly compressed in the vertical direction (simulations of specimen compression between two rigid surfaces were also conducted and found to give the same results). To obtain the nominal stress vs. nominal strain response, the total force on edge AB is monitored as a function of the applied displacement.

3.2.2. Infinite periodic structures

To subject a spatially periodic representative volume element to a macroscopic deformation gradient $\bar{\mathbf{F}}$ periodic boundary conditions are imposed on all cell boundaries such that

$$\mathbf{u}|_{\mathrm{B}}-\mathbf{u}|_{\mathrm{A}}=(\bar{\mathbf{F}}-\mathbf{I})[\mathbf{X}|_{\mathrm{B}}-\mathbf{X}|_{\mathrm{A}}]=\bar{\mathbf{H}}[\mathbf{X}|_{\mathrm{B}}-\mathbf{X}|_{\mathrm{A}}], \tag{7}$$

where A and B are two points periodically located on the RVE boundary. In Eq. (7) $\bar{\mathbf{H}}=\bar{\mathbf{F}}-\mathbf{I}$ denotes the macroscopically applied displacement gradient and $\mathbf{u}=\mathbf{x}(\mathbf{X})-\mathbf{X}$ denotes the displacement at $\mathbf{X}$. The

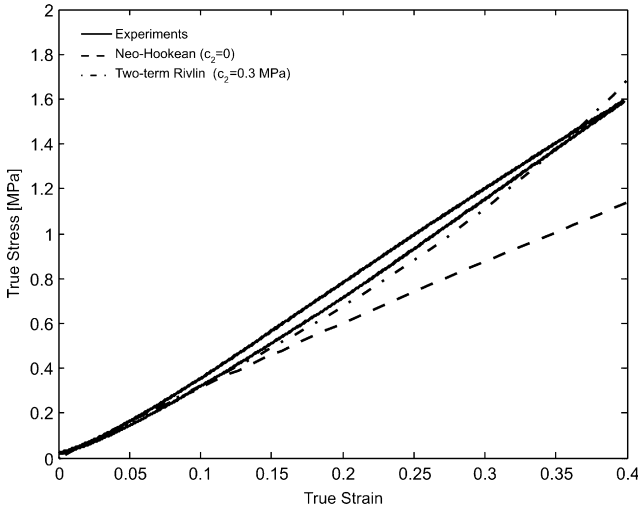

Fig. 5. True stress vs. true strain in uniaxial compression for PSM-4. Comparison between experimental data and model predictions.

macroscopic deformation is imposed by prescribing the four components of $\bar{\mathbf{H}}$, which are viewed as generalized degrees of freedom operationally applied using a set of virtual nodes. The macroscopic first Piola–Kirchoff stress tensor $\bar{\mathbf{S}}$ and the corresponding macroscopic Cauchy stress tensor $\bar{\boldsymbol{\sigma}}$ are then extracted through virtual work considerations (Danielsson et al., 2002). Rigid body motion is prevented by constraining the displacements of a single point.

Here, each representative volume element (RVE) is subjected to macroscopic uniaxial compression loading conditions

$$\bar{\mathbf{H}} = \bar{H}_{11}\mathbf{e}_1 \otimes \mathbf{e}_1 + (\lambda - 1)\mathbf{e}_2 \otimes \mathbf{e}_2, \tag{8}$$

whereby $\bar{H}_{22} = \lambda - 1$ is imposed (λ is referred to as "load parameter") and $\bar{H}_{11}$ is not prescribed and is determined by the condition $\bar{S}_{11} = 0$. $\bar{S}_{22}$ is then determined as a function of λ and the RVE nominal stress vs. nominal strain response is then computed.

3.3. Analysis of instabilities

Instability analyses of both the finite-sized periodic structures described in Section 2 and their infinite periodic counterparts were performed.

Let us consider a solid Ω (with boundary $\partial\Omega$) deformed in the X_1–X_2 plane under finite, plane strain conditions. A full Lagrangian formulation is adopted, so that the initial, undeformed configuration is taken as the reference for the incremental analysis. The rate form of the stress equilibrium in the absence of body forces is expressed as

$$\mathrm{Div}\,\dot{\mathbf{S}} = 0, \tag{9}$$

where $\dot{\mathbf{S}}$ denotes the rate of the first Piola–Kirchoff stress tensor. Here rate-independent, incrementally linear materials are considered so that the rate form of the constitutive relation can be expressed as

$$\dot{\mathbf{S}} = \mathbb{L} : \dot{\mathbf{F}} = \mathbb{L} : \mathrm{Grad}\,\mathbf{v} \tag{10}$$

where $\dot{\mathbf{F}}$ indicates the rate of the deformation gradient, $\mathbf{v}$ is the velocity and $\mathbb{L}$ is the incremental moduli tensor possessing major symmetries $\mathbb{L}_{ijkl} = \mathbb{L}_{klij}$ whose components are given by

$$\mathbb{L}_{ijkl} = \frac{\partial^2 W}{\partial F_{ij}\,\partial F_{kl}}, \tag{11}$$

W denoting the strain energy density (here given by Eq. (3)).

Let $\delta\mathbf{v}$ be an arbitrary variation of $\mathbf{v}$, which satisfies the boundary conditions on $\partial\Omega$. Integration by parts and application of the divergence theorem yields the weak form of Eq. (9)

$$\int_{\Omega} \dot{\mathbf{S}} : \mathrm{Grad}\,\delta\mathbf{v}\,\mathrm{d}V - \int_{\partial\Omega} \dot{\mathbf{t}} \cdot \delta\mathbf{v}\,\mathrm{d}S = 0, \tag{12}$$

which represents the principle of virtual work in the full Lagrangian form.

3.3.1. Eigen analysis

The stability of the periodic finite-sized specimens and the stability of the corresponding RVEs (where the RVEs are progressively increased in size) are first examined using eigenvalue analyses. A linear perturbation procedure is used and is accomplished within the commercial finite element code ABAQUS/Standard using the *BUCKLE module. The algorithm begins with the weak form of the governing equations (Eq. (12)) and is briefly summarized in Appendix A for purpose of completeness.

The eigen analyses on the finite-sized specimens are conducted after application of the loading/boundary conditions described in Section 3.2.1. Eigen analyses of the unloaded structures and of the structures after application of a modest compression yield very similar results. The analyses yield the transformed pattern (the eigenmode) and the critical nominal strain (the eigenvalue).

Refined Eigen Analyses on the RVEs are conducted on RVEs of increasing size. Taking Y as the primitive cell of the infinite periodic structure, the infinite periodic structures are modeled as RVEs consisting of $\mathbf{p}$Y cells (with $\mathbf{p} = (p_1, p_2)$) subjected to the periodic boundary conditions given by Eq. (7) . The critical value of the load parameter $\lambda^{\mathbf{p}}$ is then defined as the infimum of the load parameter λ for which a $\mathbf{p}$Y-periodic instability mode occurs. The critical value λ_{cr} is then defined as the infinimum of $\lambda^{\mathbf{p}}$ on all possible periodic unit cells $\mathbf{p}$Y. In a similar way the occurrence of higher eigenmodes are investigated. Since it is impossible to conduct bifurcation analyses of the RVE with infinitely many cells, these analyses will not yield a rigorous result. However, because of its simplicity this method is helpful to get a first understanding of the material behavior. A rigorous confirmation of the above results was then obtained performing Bloch wave analyses as described below.

3.3.2. Bloch wave analysis

Although at bifurcation the Y-periodicity may break down, the investigation of bifurcation for infinite periodic solids may still be performed on the primitive cell Y employing a Bloch wave analysis (Geymonat et al., 1993).

Let us consider the general case of an infinite periodic oblique array of holes (the square and rectangular arrays are particular cases of this more general case) with dimensions $l_1\mathbf{a}_1$ and $l_2\mathbf{a}_2$ in the two (not necessarily orthogonal) basic directions of the lattice in the undeformed configuration, as shown in Fig. 6 (left).

For the oblique lattice one possible primitive cell Y is identified by the parallelogram spanned by the vectors $l_1\mathbf{a}_1$ and $l_2\mathbf{a}_2$ (Fig. 6 (left)). However, when bifurcation occurs, the initial Y-periodicity may be broken resulting in an enlarged primitive cell $\mathbf{p}$Y consisting of $\mathbf{p} = (p_1, p_2)$ unit cells and spanned by the vectors $p_1 l_1\mathbf{a}_1$ and $p_2 l_2\mathbf{a}_2$ (Fig. 6 (right)). Thus, at bifurcation any space function ψ must satisfy the periodic conditions

$$\psi(\mathbf{X} + p_j l_j \mathbf{a}_j) = \psi(\mathbf{X}), \quad j = 1, 2, \tag{13}$$

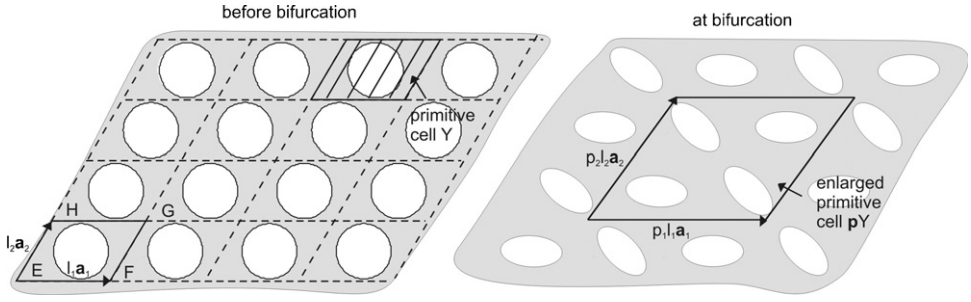

Fig. 6. Oblique lattice before and at bifurcation. In this example $p_1 = p_2 = 2$.

for any point $\mathbf{X}$ in space. Since the classical Bloch condition says that (e.g., Kittel, 1986)

$$\psi(\mathbf{X}+p_j l_j \mathbf{a}_j)=\psi(\mathbf{X})\exp[i\mathbf{k}_0\cdot(p_j l_j \mathbf{a}_j)],\quad j=1,2, \tag{14}$$

we must have

$$\exp[i\mathbf{k}_0\cdot(p_j l_j \mathbf{a}_j)]=1,\quad j=1,2, \tag{15}$$

which can only be achieved having $\mathbf{k}_0$ in the form

$$\mathbf{k}_0=k_{01}\mathbf{b}_1+k_{02}\mathbf{b}_2, \tag{16}$$

together with

$$p_1=\frac{1}{k_{01}I_1},\quad p_2=\frac{1}{k_{02}I_2}, \tag{17}$$

where the vectors $\mathbf{b}_1$, $\mathbf{b}_2$ are the reciprocal lattice vectors

$$\mathbf{b}_1=2\pi\frac{\mathbf{a}_2\times\mathbf{e}}{A},\quad \mathbf{b}_2=2\pi\frac{\mathbf{e}\times\mathbf{a}_1}{A}, \tag{18}$$

with $A=||\mathbf{a}_1\times\mathbf{a}_2||$ and $\mathbf{e}=(\mathbf{a}_1\times\mathbf{a}_2)/A$.

Operationally, to obtain the bifurcation modes of the infinite periodic solid, the primitive cell Y is considered together with velocities given by the Bloch type relation

$$\mathbf{v}(\mathbf{X}+l_j\mathbf{a}_j)=\mathbf{v}(\mathbf{X})\exp[i\mathbf{k}_0\cdot(I_j\mathbf{a}_j)],\quad j=1,2 \tag{19}$$

with $\mathbf{k}_0=k_{01}\mathbf{b}_1+k_{02}\mathbf{b}_2$ lying in the unit cell of the reciprocal lattice, i.e. $0\leqslant k_{01}<1/l_1$ and $0\leqslant k_{02}<1/l_2$ and $\mathbf{v}$ being in general a complex-valued function.

Eq. (19) implies that the velocities $\mathbf{v}$ and tractions $\dot{\mathbf{t}}=\dot{\mathbf{S}}\,\mathbf{n}$ evaluated along opposite sides of the primitive cell Y (Fig. 6 (left)) are related through

$$\mathbf{v}|_{\mathrm{FG}}=d_1\mathbf{v}|_{\mathrm{EH}},\quad \mathbf{v}|_{\mathrm{HG}}=d_2\mathbf{v}|_{\mathrm{EF}},\quad \mathbf{v}|_{\mathrm{F}}=d_1\mathbf{v}|_{\mathrm{E}},\quad \mathbf{v}|_{\mathrm{H}}=d_2\mathbf{v}||_{\mathrm{E}},\quad \mathbf{v}|_{\mathrm{G}}=d_1d_2\mathbf{v}|_{\mathrm{E}}, \tag{20}$$

and

$$\dot{\mathbf{t}}|_{\mathrm{FG}}=-d_1\dot{\mathbf{t}}|_{\mathrm{EH}},\quad \dot{\mathbf{t}}|_{\mathrm{HG}}=-d_2\dot{\mathbf{t}}|_{\mathrm{EF}}, \tag{21}$$

where $d_j=\exp[i2\pi k_{0j}l_j]$ and the uppercase subscripts "IJ" denote points along side "IJ" and act to pair, for example, a point on side EH with its point (the point with the same initial vertical location) on side FG.

Following Åberg and Gudmundson (1997), since most commercial finite element codes including ABAQUS do not directly handle complex valued displacements, all of the fields $\mathbf{w}$ are split into a real and imaginary parts

$$\mathbf{w}=\mathbf{w}^{\mathrm{Re}}+\mathbf{i}\mathbf{w}^{\mathrm{Im}}. \tag{22a}$$

By substitution of Eq. (22a) into Eq. (12), the principle of virtual work splits into two uncoupled equations for the real and imaginary parts, respectively, with boundary conditions given by Eqs. (20) and (21). Since the real and imaginary parts are uncoupled in the equilibrium equations, the problem is solved using two identical finite element meshes for the primitive cell, one for the real part and one for the imaginary part. The two meshes are coupled by the displacement boundary conditions given by Eq. (20) (boundary conditions given in Eq. (21) are automatically satisfied when such boundary displacements are applied).

Finite element discretization of Eq. (12) yields

$$\begin{bmatrix}\mathbf{K} & 0\\ 0 & \mathbf{K}\end{bmatrix}\begin{bmatrix}\hat{\mathbf{v}}^{\mathrm{Re}}\\ \hat{\mathbf{v}}^{\mathrm{Im}}\end{bmatrix}=\begin{bmatrix}\dot{\mathbf{f}}^{\mathrm{Re}}\\ \dot{\mathbf{f}}^{\mathrm{Im}}\end{bmatrix}, \tag{22b}$$

where $\mathbf{K}$ represents the full stiffness matrix for the primitive cell and $\hat{\mathbf{v}}^{\mathrm{Re}}$, $\hat{\mathbf{v}}^{\mathrm{Im}}$, $\dot{\mathbf{f}}^{\mathrm{Re}}$ and $\dot{\mathbf{f}}^{\mathrm{Im}}$ are the nodal displacement and force vectors corresponding to the discretization of the real and imaginary part of $\mathbf{v}$ and $\dot{\mathbf{t}}$, respectively. Application of the boundary conditions (20) and (21) to Eq. (22b) and static condensation of the degrees of freedom belonging to the nodes on the edges HG and FG (the process is detailed in

Appendix B) yields

$$\tilde{\mathbf{K}}\begin{bmatrix}\hat{\mathbf{v}}_a^{Re}\\ \hat{\mathbf{v}}_a^{Im}\end{bmatrix}=0, \tag{23}$$

where the matrix $\tilde{\mathbf{K}}$ is a symmetric function of $\mathbf{k}_0$, $\tilde{\mathbf{K}}=\tilde{\mathbf{K}}(\mathbf{k}_0)$ and $\hat{\mathbf{v}}_a^{Re}=[\hat{\mathbf{v}}_{EF}^{Re}\ \ \hat{\mathbf{v}}_{EH}^{Re}\ \ \hat{\mathbf{v}}_E^{Re}]^T$ and $\hat{\mathbf{v}}_a^{Im}=[\hat{\mathbf{v}}_{EF}^{Im}\ \ \hat{\mathbf{v}}_{EH}^{Im}\ \ \hat{\mathbf{v}}_E^{Im}]^T$. Since Eq. (23) represents an eigenvalue problem, the Bloch wave stability analysis of the infinite periodic solid requires finding the minimum value λ_c of the loading parameter λ for which the lowest eigenvalue of $\tilde{\mathbf{K}}(\mathbf{k}_0)$ is zero. The periodicity $\mathbf{p}$ of the solid at bifurcation is then obtained from Eq. (17).

We further observe that two different types of bifurcation eigenmodes are mapped in the neighborhood of the origin $\mathbf{k}_0=(0,0)$:

- for $\mathbf{k}_0=0$ a periodic "local" mode is found with $\mathbf{p}=(1,1)$;
- for $\mathbf{k}_0\to 0$ a "global" long wavelength mode is obtained with wavelength much larger than the unit cell size.

The latter case corresponds to loss of ellipticity at the macroscopic scale (Geymonat et al., 1993).

3.3.3. Loss of ellipticity

The macroscopic level loss of ellipticity is assessed by determining the response of the macroscopic (homogenized) tangent moduli of the solid $\mathbb{L}^H$

$$\dot{\tilde{\mathbf{S}}}=\mathbb{L}^H\dot{\bar{\mathbf{F}}}, \tag{24}$$

relating the average rate of the macroscopic deformation gradient $\dot{\bar{\mathbf{F}}}$ to the average rate of the macroscopic first Piola–Kirchoff stress tensor $\dot{\tilde{\mathbf{S}}}$. The onset condition of macroscopic instability is examined by investigating the conditions for which

$$A_{ik}m_im_k=0, \tag{25}$$

where **A(N)** is the acoustic tensor defined as

$$A_{ik}=\mathbb{L}_{ijkl}N_jN_1. \tag{26}$$

Operationally, after determining the principal solution for each load parameter λ, the components of $\mathbb{L}^H$ are identified by subjecting the unit cells to four independent linear perturbations of the macroscopic deformation gradient, calculating the corresponding averaged stress components and comparing to Eq. (24). This is easily calculated due to the virtual node methodology used to enforce the boundary conditions described earlier. Then loss of ellipticity is examined by checking condition (25) at every $\pi/720$ radian increment.

Notice that the macroscopic critical load is always greater than or equal to the microscopic critical load, with the equality achieved when, in the microscopic analysis, the critical load is obtained for $\mathbf{k}_0\to 0$.

3.4. Post-transformation analysis

Load–displacement analyses for both the finite-sized and infinite periodic structures were performed with ABAQUS/Standard thus capturing the post-transformation behavior. After determining the pattern transformation (the lowest eigenmode) from the eigen analysis, an imperfection in the form of the most critical eigenmode is introduced into the mesh. The mesh is perturbed by the first eigenmode $\boldsymbol{\phi}_1$, scaled by the scale factor w,

$$\Delta\mathbf{x}_0=w\frac{d_x+d_y}{2}\boldsymbol{\varphi}_1. \tag{27}$$

Thus, the perturbation $\Delta\mathbf{x}_0$ introduced into the mesh is a fraction of the averaged center-to-center distance between the voids (d_x and d_y denoting the horizontal and vertical center-to-center distance, respectively). The studies reported here use scale factors w of 0.05%, 0.1%, 0.5%, and 1%. For all levels of imperfection the same transformed pattern was obtained. For the case of small imperfections, the response is found to grow quickly near the critical load, introducing a rapid change in behavior. On the other hand, for the largest

imperfections, the post-transformation response grows steadily prior to the critical load so that the transition into post-transformed behavior is smooth.

4. Modeling results

Modeling results for both the finite size specimens and their infinite counterparts will be presented for each geometry. First, the eigenmodes of the specimens will be investigated. Then the macroscopic nominal stress vs. nominal strain behavior and corresponding deformed microstructures will be shown at various levels of imposed macroscopic strain.

4.1. Circular holes on a square lattice

4.1.1. Analysis of instabilities

Instability analyses of the cases of circular holes arranged on a square lattice (Specimens 1 and 2) were performed using eigen analyses (Section 3.3.1) for the finite-sized periodic solids and both Refined Eigen Analyses (Section 3.3.1) and Bloch wave analyses (Section 3.3.2) for their infinite periodic counterparts. All the analyses were performed considering both a Neo-Hookean and two-term Rivlin behavior for the elastomeric matrix. The differences between the results obtained using the two material models were found to be negligible.

4.1.1.1. Finite-sized periodic structure. Fig. 7 shows the first four eigenmodes for Specimen 1 (Specimen 2 is characterized by the same first three modes and a slightly different mode four).

The first eigenmode of the finite-sized specimen clearly corresponds to the transformed pattern observed in the compression tests (Fig. 2 (right)). The transformation occurs throughout the specimen with the exception of the rows neighboring the boundary constraint. Modes 2–4 exhibit periodic pockets of the Mode 1 pattern where these modes are clearly the result of interactions between the local instabilities and the boundaries; hence, the critical stress levels for these higher modes are not significantly higher than those of Mode 1. Thus, the eigen analyses further confirm the pattern transformations to be the result of elastic instability events. The modal analyses also suggest the ability to trigger alternative pattern transformations by suppressing the lower modes; for example, a compliant elastic inclusion could act to suppress the Mode 1 pattern and hence favor the Mode 2 pattern of the RVE; alternatively, preferentially placed inclusions could create patterns of alternating transformed and non-transformed domains (Prange et al., 2007; Boyce et al., 2008).

4.1.1.2. Infinite periodic structures. Refined Eigen Analyses of RVEs consisting of $m \times m$ ($m = 1, 2, \ldots, 10$) primitive cells were performed in ABAQUS using the general periodic boundary conditions (Eq. (7)) on the enlarged cell. Fig. 8 shows the first and second eigenmodes obtained for enlarged $\mathbf{p}$Y cells with $\mathbf{p} = (2, 2)$, $\mathbf{p} = (5, 5)$ and $\mathbf{p} = (6, 6)$. It can be seen from the figure that the eigenmodes vary with the number of primitive cells in the RVE; however, all the RVEs with $2m \times 2m$ ($m = 1, 2, \ldots$) primitive cells have the same first eigenmode.

Fig. 9 shows the Refined Eigen Analysis results for the nominal stress at instability (both the first and the second eigenmodes are considered) and the RVE size. For the first eigenmode, the stress at instability is

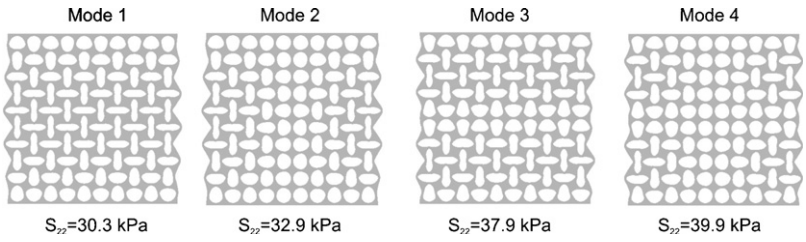

Fig. 7. Eigenmodes and eigenvalues (critical stress) for the finite-size specimen for Specimen 1.

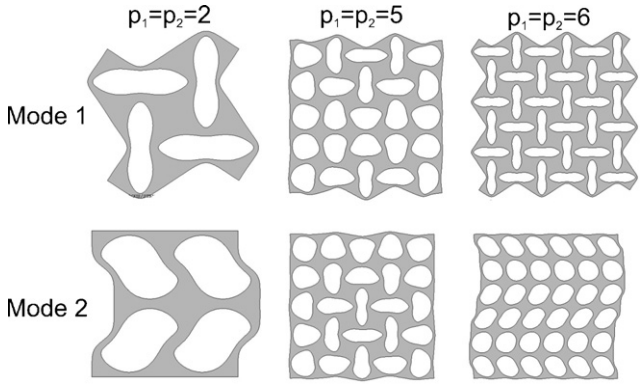

Fig. 8. Eigenmodes for enlarged **p**Y cells with $\mathbf{p} = (2, 2)$, $\mathbf{p} = (5, 5)$ and $\mathbf{p} = (6, 6)$.

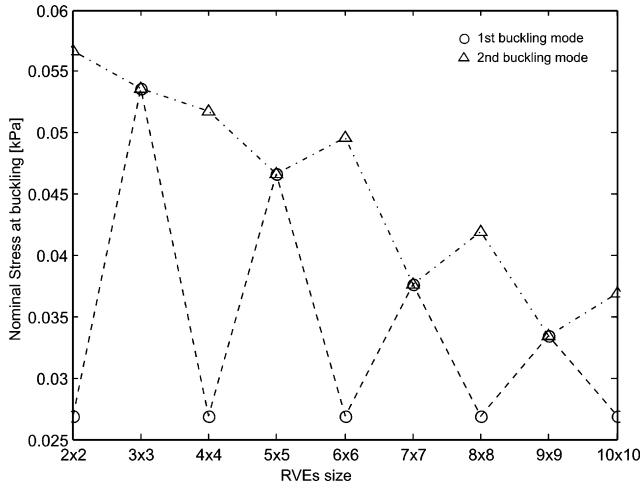

Fig. 9. Critical stresses vs. RVE size for Specimen 1 (Specimen 2 is characterized by the same trend).

observed to converge to that of $2m \times 2\,\mathrm{m}$ ($m = 1, \ldots, 5$) primitive cells asymptotically, so that a periodicity $\mathbf{p} = (2, 2)$ is expected. Differently, the second eigenmode of "even" cells exhibits a critical stress that monotonically decreases with increasing the RVE size and a wavelength equal to the RVE cell length, thus suggesting picking up a "global" mode.

To rigorously confirm the findings from the Refined Eigen Analyses, Bloch wave analyses were performed on the primitive cell (Fig. 1 (center)) of the infinite counterparts of both Specimens 1 and 2. During compression simulations, a critical instability is detected at an engineering strain of 0.03 and 0.08 for Specimens 1 and 2, respectively. When the critical instability occurs, the Y-periodicity is broken and an enlarged primitive cell **p**Y with $\mathbf{p} = (2, 2)$ is found, as shown in Fig. 10. The corresponding critical stresses are found to be 30 and 114 kPa for Specimens 1 and 2, respectively. These values are slightly larger than the nominal stresses at critical instability predicted by the Refined Eigen Analysis (27 and 88 kPa). This difference in the prediction of the critical load is related to the fact that the Refined Eigen Analysis computation was performed on the unloaded structure, whereas the Bloch wave analysis accounts for the effects of the loading prior instability. This discrepancy indicates that the relatively modest strains involved in these deformations have a slight effect on the configuration.

After the first eigenmode at an engineering strain of -0.055 and -0.1 for Specimens 1 and 2, respectively (as shown in Table 1), loss of ellipticity for the homogenized tangent moduli is encountered, leading to a "global" eigenmode.

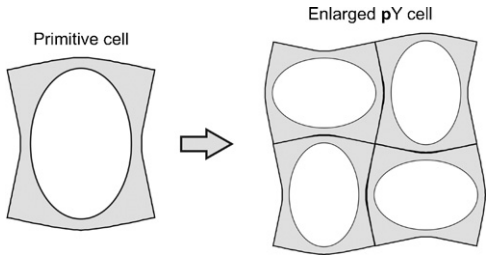

Fig. 10. Eigenmode of the microscopic bifurcation instability for the infinite counterpart of Specimen 1 as predicted by the Bloch wave analysis (Specimen 2 is characterized by a similar eigenmode).

Table 1
Instability strain levels for Specimens 1 and 2 as predicted by the Bloch wave analysis and the loss of ellipticity analysis

	Engineering strain at microscopic instability	Nominal stress at microscopic instability (kPa)	Engineering strain at macroscopic instability
Specimen 1	0.03	30	0.055
Specimen 2	0.08	116	0.1

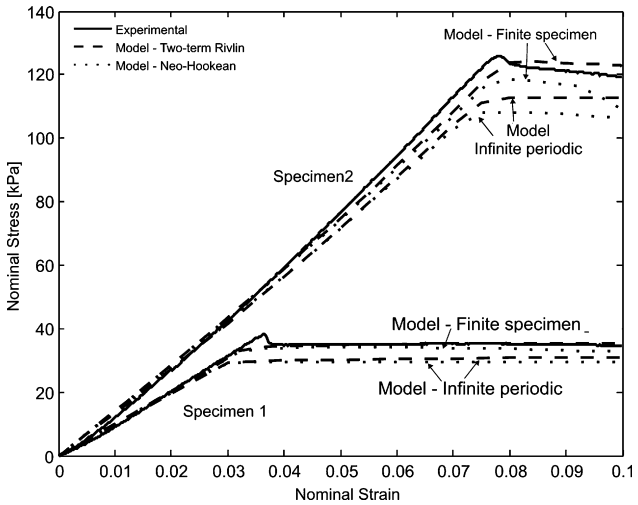

Fig. 11. Nominal stress vs. nominal strain curves for Specimens 1 and 2 (square arrays of circular holes with 9.97 and 10.97 mm center-to-center spacing) showing experimental and computational (Neo-Hookean and two-term Rivlin model with $w = 0.05\%$) results.

4.1.2. Post-transformation analysis

Post-transformation analyses were conducted by introducing a geometrical imperfection with the form of the first eigenmode to preferentially activate the first mode during simulation of the compression test of both the finite-sized specimen and its infinite counterpart. For the analysis of the infinite periodic solid as suggested by the instability analyses a **p**Y cell with $\mathbf{p} = (2, 2)$ is used. Excellent quantitative agreement is obtained between the stress–strain results of the finite-sized model calculation and those from the experiment for both Specimens 1 and 2 as shown in Fig. 11. For both cases, the infinite periodic solid results exhibit an earlier departure from linearity than those from the finite-sized model since the former do not capture the influence of the boundary conditions. Fig. 11 shows that the stress–strain behaviors for the two different material models (Neo Hookean and two-term Rivlin model) presented in Section 3.1 are almost identical. The strain levels attained during the compression test are low enough that the neo-Hookean model captures the behavior very well. An imperfection analysis was also conducted using the scale factor w of 0.05%, 0.1%, 0.5%, and 1% (the results are not reported for the sake of brevity); in all cases the transformed pattern is obtained.

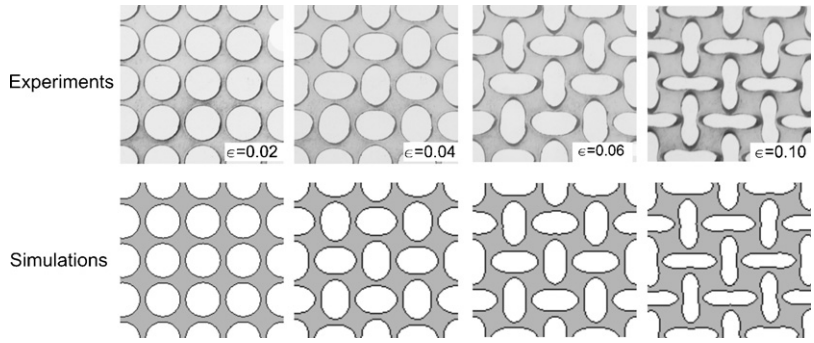

Fig. 12. Experimental (top) and numerical (bottom) images of Specimen 1 (square lattice with 9.97 mm center-to-center spacing) at different levels of macroscopic strain: 2%, 4%, 6%, and 10%.

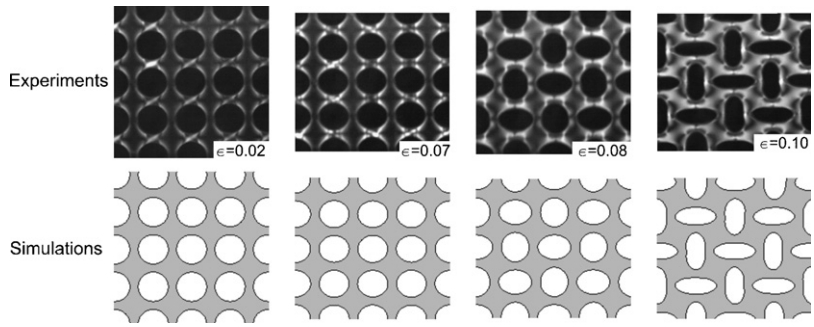

Fig. 13. Experimental (top) and numerical (bottom) images of Specimen 2 (square lattice with 10.97 mm center-to-center spacing) at different levels of macroscopic strain: 2%, 7%, 8%, and 10%.

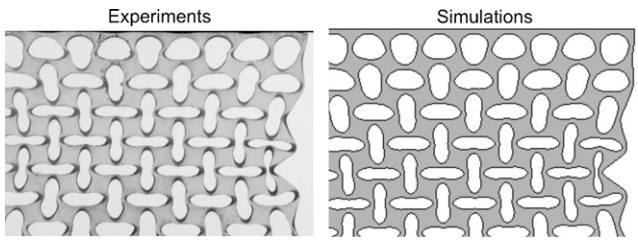

Fig. 14. Experimental (left) and numerical (right) images of Specimen 1 at a strain of 0.10.

There is excellent agreement between the model predictions and the experimental images of the pattern evolutions with strain for both Specimens 1 and 2 as shown in Figs. 12 and 13. The homogeneous compression of the circular array during the linear regime of the stress–strain behavior, the pattern transformation at the critical stress, and the accentuation of the new alternating elliptical pattern with ongoing strain are all captured.

For completeness, a nearly full view (the top and bottom row of the experiment are obscured by the test fixtures) of the full specimen and the corresponding simulation at a strain of 0.10 are shown in Fig. 14 again demonstrating excellent agreement between simulation and experimental results.

Here, we emphasize the uniformity and robustness of the transformation in the elastomeric periodic solids where the change occurs essentially uniformly throughout the structure (as demonstrated in our experiments and simulations). In other words, the instability does not localize deformation in a row or diagonal band, but instead results in a homogeneous pattern transformation throughout the structure. The transformed structure is then further accentuated with continuing deformation and this occurs at nearly constant load. Further, the entire process is reversible and repeatable. This stress–strain behavior is characteristic of superelastic behavior.

4.2. Elliptical holes on a rectangular lattice

4.2.1. Analysis of instabilities

Following the approach used for the analysis of the square array of circular holes, instability analyses of both the finite-sized specimen and its infinite counterpart have been performed. Also in this case the differences between the results obtained using the Neo-Hookean model and the two-term Rivlin model for the elastomeric matrix were found to be negligible, so that only the results pertaining the two-term Rivlin model are reported for sake of brevity.

4.2.1.1. Finite-sized periodic structures. The first four eigenmodes of the finite-sized specimen are shown in Fig. 15 for compression perpendicular to the major axis and in Fig. 16 for compression parallel to the major axis of the ellipses. Similar to the case of the square array of circular holes, the higher modes of the finite-sized specimen contain pockets of the Mode 1 pattern and the corresponding critical stress levels are close to that of Mode 1. For the case of compression parallel to the major axis of the ellipses, the critical instability has found to be strongly influenced by the preloading. Computation of the eigenmodes on the unloaded structures yields a wavy eigenmode, whereas the pattern observed during the experimental tests (Fig. 3 (right)) is correctly captured applying a preload of 15 kPa before performing the eigen analysis in ABAQUS, as shown in Fig. 16.

4.2.1.2. Infinite periodic structures. Refined Eigen Analyses were performed for the infinite periodic solid compressed in the direction both perpendicular and parallel to the major axes of the ellipses. The first and second eigenmodes and the relationship between the critical stress and the RVE size are reported in Figs. 17 and 18 for the case of compression in the direction perpendicular to the ellipses' major axes and in Figs. 19 and 20 for the case of compression in the direction parallel to the ellipses' major axes.

When the solid is compressed in the direction perpendicular to the major axes of the ellipses, similarly to the case of the square array of circular voids, the analyses suggest a critical eigenmode with a periodicity $\mathbf{p} = (2, 2)$, followed by a "global" mode.

Differently, for the case of compression of the RVE in the direction parallel to the ellipse major axes, the experimentally observed transformed pattern is not captured by the eigenmodes. In addition, Fig. 20 shows that the critical stress levels for the first two eigenmodes are quite close in magnitude and are independent of the RVE size. Thus a "global" mode is expected in this case as critical instability.

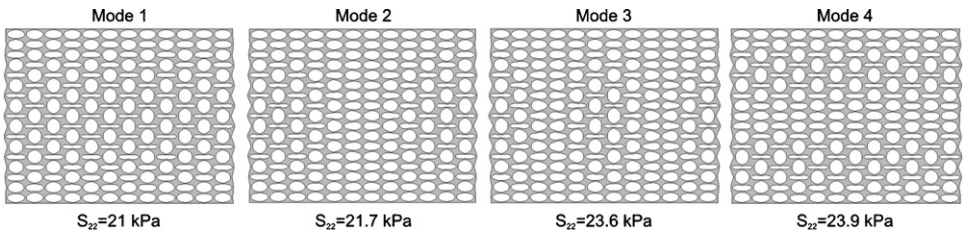

Fig. 15. Eigenmodes and eigenvalues (critical stress) for the finite-size specimen compressed in the direction perpendicular to the ellipses' major axes.

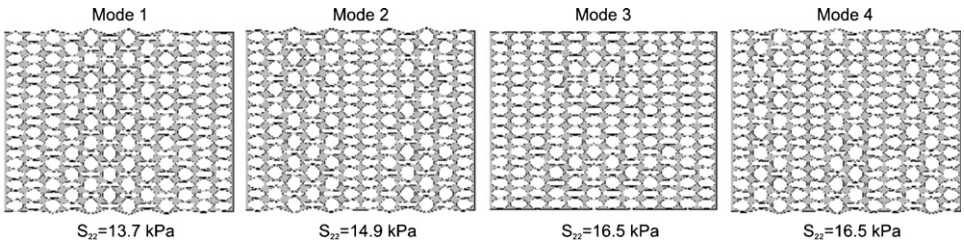

Fig. 16. Eigenmodes and eigenvalues (critical stress) for the finite-size specimen compressed in the direction parallel to the ellipses' major axes.

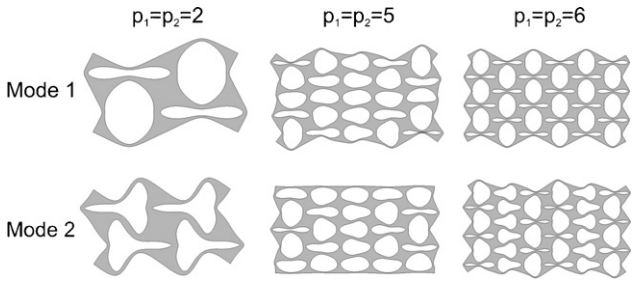

Fig. 17. Eigenmodes for enlarged **pY** cells compressed in the direction perpendicular to the ellipses' major axes. Results are reported for $\mathbf{p} = (2, 2)$, $\mathbf{p} = (5, 5)$ and $\mathbf{p} = (6, 6)$.

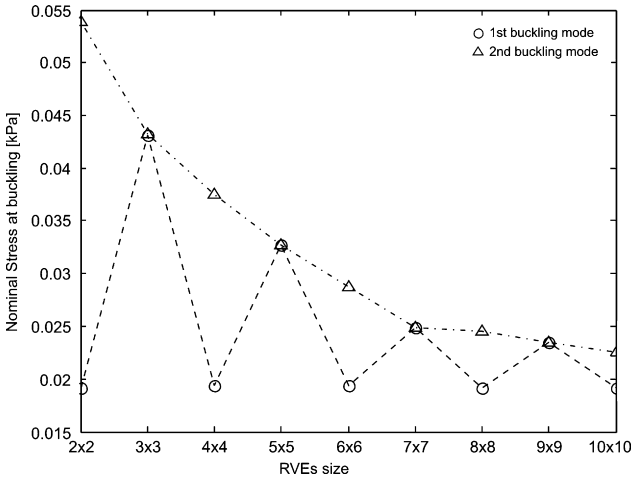

Fig. 18. Critical stress vs. RVE size for compression in the direction perpendicular to the ellipses' major axes.

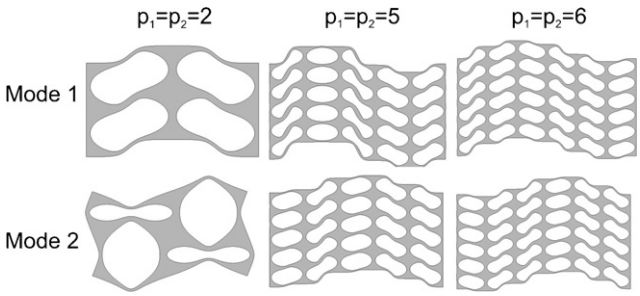

Fig. 19. Eigenmodes for enlarged **pY** cells compressed in the direction parallel to the ellipses' major axes. Results are reported for $\mathbf{p} = (2, 2)$, $\mathbf{p} = (5, 5)$ and $\mathbf{p} = (6, 6)$.

Bloch wave analyses performed on the primitive cells confirm that when the solid is compressed in the direction perpendicular to the major axes of the ellipses a critical instability is detected with a periodicity $\mathbf{p} = (2, 2)$ at an engineering strain of 0.033 (Fig. 21), followed by a macroscopic instability at a strain of 0.043 (Table 2). For compression in direction parallel to the major axes no microscopic instability is detected prior to macroscopic instability which would occur at an engineering strain of 0.0165.

4.2.2. Post-transformation analysis

An imperfection in the form of the first eigenmode was placed in the mesh to preferentially activate the first mode during the compression test on both the finite-sized specimen and RVE models containing 2×2

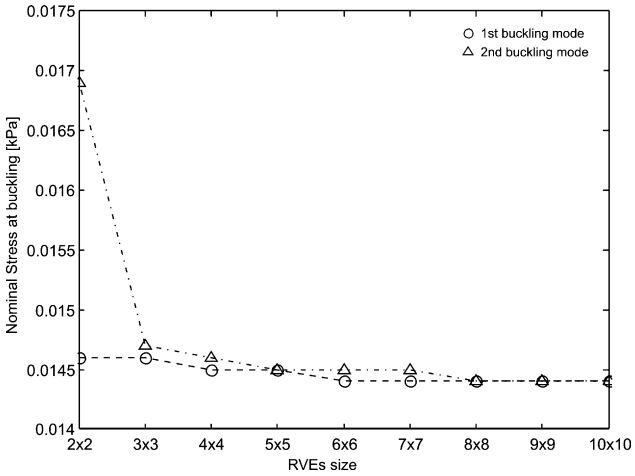

Fig. 20. Critical stress vs. RVE size for compression in the direction parallel to the ellipses' major axes.

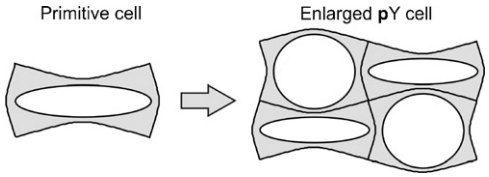

Fig. 21. Eigenmode of the microscopic bifurcation instability for the infinite counterpart of Specimen 3 compressed in the direction perpendicular to the ellipses' major axes as predicted by the Bloch wave analysis.

Table 2
Instability strain levels for Specimen 3 compressed in the direction parallel and perpendicular to the ellipses' major axes as predicted by the Bloch wave analysis and the loss of ellipticity analysis

	Engineering strain at microscopic bifurcation	Engineering strain at macroscopic bifurcation
Perpendicular	−0.033	−0.043
Parallel	–	−0.017

primitive cells, except for the case of the RVE compressed in direction parallel to the major axes of the ellipses. In the latter case no defects were introduced into the mesh, since macroscopic instability is encountered first during uniaxial compression. Fig. 22 shows excellent agreement between the finite-sized model predictions and the experimental results, whereas Figs. 23 and 24 show excellent agreement between the model predictions and the experimental images of the pattern evolutions with strain for both loading cases.

4.3. Circular holes on an oblique lattice

4.3.1. Analysis of instabilities

Following the approach used for the analysis of the square array of circular voids and the rectangular array of elliptical voids, eigen analyses of the finite-sized specimen and enlarged RVEs as well as Bloch wave analyses on the primitive cell have been performed. The results reported here refer to the case of a two-term Rivlin model used for the elastomeric matrix. Similar results were obtained when the matrix is modeled using the Neo-Hookean model.

4.3.1.1. Finite-sized periodic structures. Fig. 25 shows the first four eigenmodes of Specimen 4 (Specimen 5 is characterized by the same first three eigenmodes and a slightly different mode four). The first mode clearly

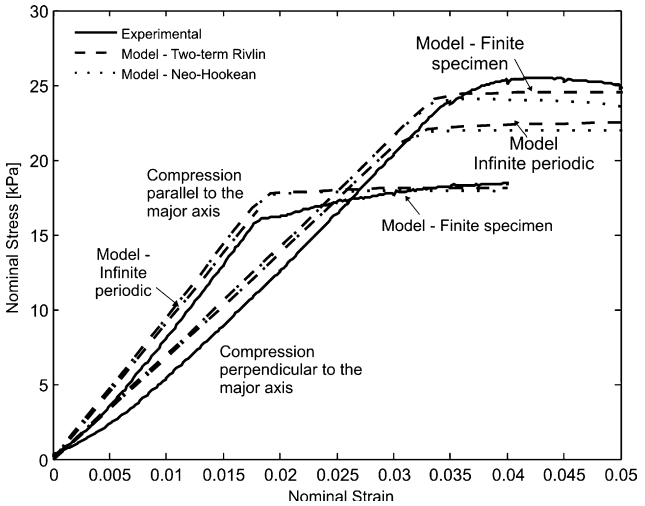

Fig. 22. Nominal stress vs. nominal strain curves for the rectangular array of elliptical holes compressed in the direction perpendicular to the major axis and the direction parallel to the major axis showing experimental and computational (finite-sized model and RVE model) results.

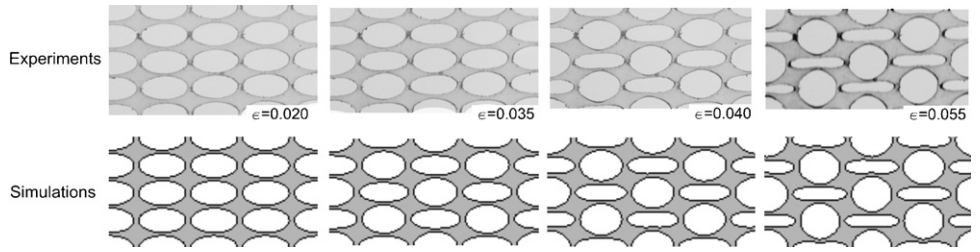

Fig. 23. Experimental (top) and numerical (bottom) images of the rectangular lattice of elliptical holes compressed in the direction perpendicular to the major axis at different levels of macroscopic strain: 2%, 3.5%, 4%, and 5.5%.

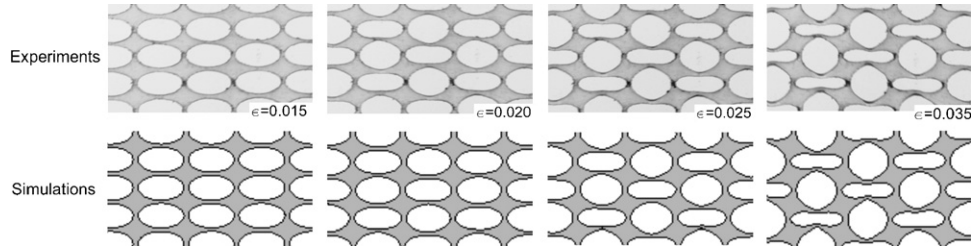

Fig. 24. Experimental (top) and numerical (bottom) images of the rectangular lattice of elliptical holes compressed in the direction parallel to the minor axis at different levels of macroscopic strain: 1.5%, 2%, 2.5%, and 3.5%.

captures the experimentally observed transformed pattern. The higher modes of the finite-sized specimen contain rows of the Mode 1 pattern. The edges of the oblique array specimens are sliced through the voids (see Fig. 1) and hence there is not an edge boundary layer of solid giving a lateral constraint on any instability.

4.3.1.2. Infinite periodic structures. Refined Eigen Analyses were performed in ABAQUS on enlarged **pY** cells consisting of $1 \times m$ ($m = 1, 2, \ldots, 10$) primitive cells applying periodic boundary conditions (Eq. (7)) to the outer boundaries of the **pY** cells. Fig. 26 clearly shows that the stress at instability for the first eigenmode converges to that of $1 \times 2m$ ($m = 1, \ldots, 5$) primitive cells asymptotically, suggesting a periodicity $\mathbf{p} = (1, 2)$.

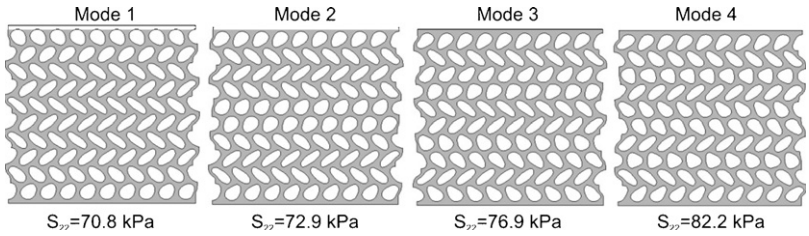

Fig. 25. Eigenmodes and eigenvalues (critical stress) for the finite-size specimen for Specimen 4.

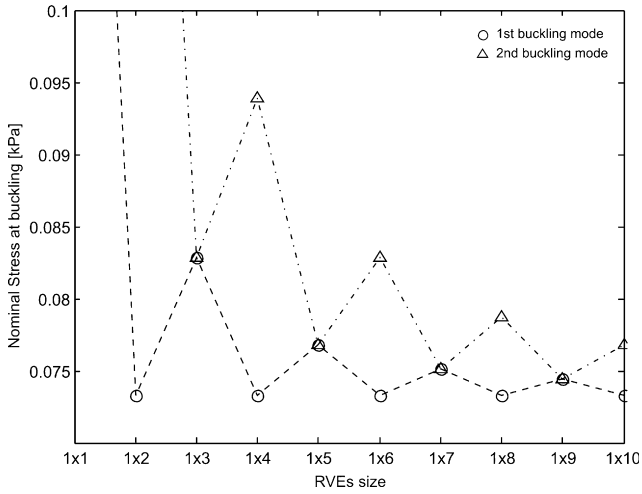

Fig. 26. Critical stress vs. RVE size obtained in ABAQUS for Specimen 4.

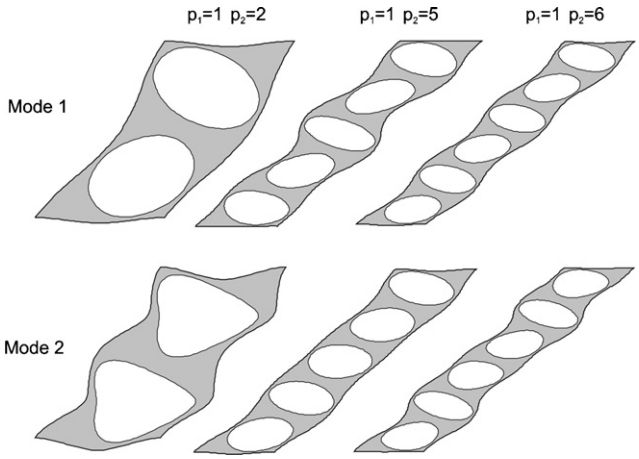

Fig. 27. Eigenmodes for enlarged **p**Y cells for Specimen 4 (Specimen 5 is characterized by similar eigenmodes). Results are reported for $\mathbf{p} = (1, 2)$, $\mathbf{p} = (1, 5)$ and $\mathbf{p} = (1, 6)$.

Differently, the stress at instability of the second mode monotonically decreases with increasing the RVE size, becoming closer to that of the first eigenmode. Fig. 27 shows the first and second eigenmodes for enlarged **p**Y cells with $\mathbf{p} = (1, 2)$, $\mathbf{p} = (1, 5)$ and $\mathbf{p} = (1, 6)$. The second eigenmode corresponds to a slight variation of the first one.

Bloch wave analyses were performed on the primitive cell (Fig. 1 (center)). The analyses confirmed that the critical instability, occurring at a compressive strain of 0.13 and 0.18 for Specimens 4 and 5, respectively, has a

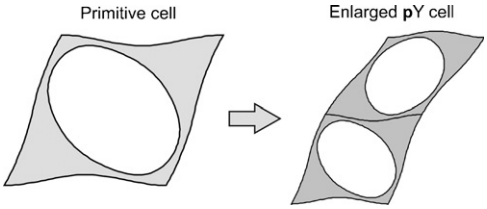

Fig. 28. First eigenmode of the microscopic bifurcation instability for the infinite counterpart of Specimen 4 (Specimen 5 is characterized by the same first eigenmode) as predicted by the Bloch wave analysis.

Table 3
Instability strain levels for Specimens 4 and 5 as predicted by the Bloch wave analysis and the loss of ellipticity analysis

	Engineering strain at microscopic instability	Nominal stress at microscopic instability (kPa)	Engineering strain at macroscopic instability
Specimen 4	0.13	91	0.30
Specimen 5	0.18	204	0.32

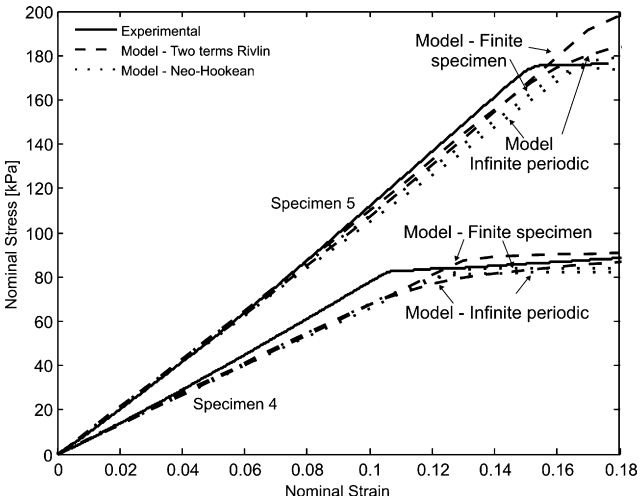

Fig. 29. Nominal stress vs. nominal strain curves for Specimens 4 and 5 (oblique array of circular voids) showing experimental and computational (finite-sized model and RVE model) results.

periodicity $\mathbf{p} = (1, 2)$ as shown in Fig. 28. Loss of ellipticity is then encountered at a compressive engineering strain of 0.30 and 0.32 for Specimens 4 and 5, respectively (Table 3).

4.4. Post-transformation analysis

An imperfection in the form of the first eigenmode was introduced into the mesh to activate the first mode during simulation of the compression test. Fig. 29 provides a direct comparison between the numerical and experimental stress–strain results, showing excellent agreement between the model predictions and the experimental results. The 1×2 enlarged RVE exhibits a response almost equal to that characterizing the finite-sized model, since the lateral boundaries are not influencing the behavior of the finite-sized specimen.

Finally, Fig. 30 shows the comparison between the model predictions and the experimental images of the pattern evolutions with strain for Specimen 4 and excellent agreement is found between model predictions and experimental results.

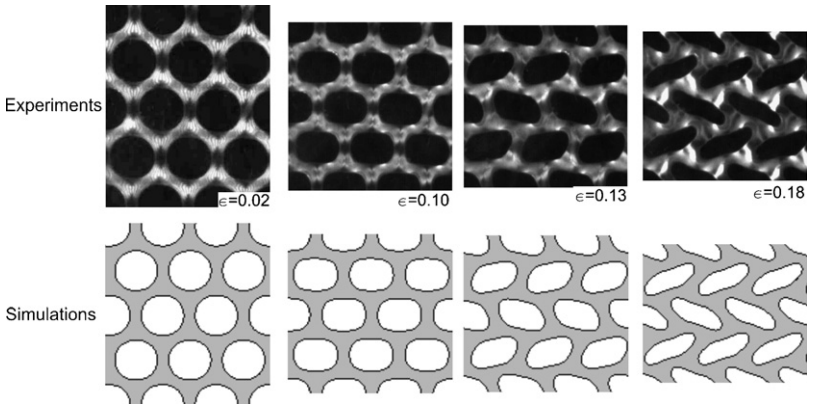

Fig. 30. Experimental (top) and numerical (bottom) deformed images for Specimen 4 at different levels of macroscopic strain: 2%, 10%, 13%, and 18%.

5. Conclusions

The mechanics of deformation of several two-dimensional periodic elastomeric cellular structures have been studied, revealing that deformation can be used to trigger dramatic homogeneous pattern transformations. The nonlinear stress–strain behavior of cellular solids has attracted much interest, since these materials provide superior energy absorption opportunities. Under compression cellular solids exhibit a nonlinear stress–strain behavior with departure from a linear response to a plateau stress caused by an initial structural instability that develops inside the cell microstructure. Upon reaching a critical stress level, the deformation is observed to localize into bands that progress through the structure at relatively constant stress up to large strains (e.g., Gibson and Ashby, 1997; Papka and Kyriakides, 1994, 1998a, b, 1999a; Triantafyllidis and Schraad, 1998; Ohno et al., 2002; Tantikom et al., 2005a, b).

Here, purely elastic periodic structures are analyzed. Our experimental tests clearly show that in the periodic elastomeric cellular solids, the initial instability leads to a uniform pattern transformation that develops simultaneously throughout the material. Several periodic elastomeric structures have been analyzed, each showing a uniform transformation to a pattern that depends on the geometry of the initial microstructure. This indicates the interesting possibility of tuning the initial microstructure to obtain the desired transformed pattern. Numerical analyses show that the pattern transformations are the result of local elastic instabilities and therefore they are reversible and repeatable. The reversible and repeatable nature of the transformations has also been demonstrated experimentally. The eigenvalue analyses also suggest the ability to trigger alternative pattern transformations by suppressing lower modes, for example replacing some of the holes with inclusions. The effect has been demonstrated at millimeter length scales but should also persist at the micro or even nano scales. There is increasing interest for the creation and use of periodic structures to achieve unique material and surface properties and attributes. Periodic structures can be used as phononic crystals, where the microstructure is designed to control properties and propagation of sound. Using appropriate materials and pattern length scales, periodic structures can be used as photonic crystals, where the microstructure is designed to control the flow of light. Periodic submicron structures have also been found to be an important governing factor in the hydrophobic character of surfaces, where the microtextures modify the material wettability. Our work indicates the exciting prospect of using the dramatic and homogeneous mechanical deformation behavior observed in elastomeric periodic structures to control attributes that depend on the periodic pattern (Bertoldi and Boyce, 2008). In the case considered here we have the distinct possibility of fabricating an optical or an acoustic switch which could be used, for example, to direct light or sound in a controlled manner, since the pattern transformation event is nonlinear in nature and thus very small changes in macroscopic strain produce a sudden transformation in the pattern. Our work also indicates the exciting prospect of a technological advance by imprinting complex patterns during the fabrication process using a minimum number of developmental steps. For example, this could be done by heating a stiff substrate above its glass transition temperature, applying a load to trigger the transformation, and then freezing the pattern in by

cooling. This technique could be taken one step further whereby a reheating step would recover the initial pattern (due to the shape memory effect in amorphous polymers). The experiments and simulations presented here have revealed and demonstrated novel deformation-induced pattern transformation in two-dimensional periodic structures; analogous deformation-induced transformations should be expected in three-dimensional periodic structures.

Acknowledgments

The work of TM is supported by an EPSRC 'Senior Fellowship' during a visit to MIT. The authors acknowledge the use of experimental facilities at the Department of Mechanical Engineering and the Institute for Soldier Nanotechnologies (ISN) at MIT and support from the Gail E. Kendall Professorship. A portion of this work was sponsored by ISN.

Appendix A. Eigen analysis in ABAQUS

Beginning with the principle of virtual work as expressed in Eq. (12) of the main text, choosing the current configuration as reference configuration and using the relationship $\mathbf{S}=\boldsymbol{\tau}\mathbf{F}^{-\mathrm{T}}$, where $\mathbf{S}$ is the first Piola–Kirchoff stress, $\boldsymbol{\tau}$ is the Kirchoff stress, and $\delta\mathbf{v}=\delta\dot{\mathbf{F}}=\delta\mathbf{L}$, $\delta\mathbf{L}$ the virtual velocity gradient, the first term in Eq. (12) takes the form

$$\int_{\Omega}\dot{\mathbf{S}}:\operatorname{grad}\delta\mathbf{v}\,\mathrm{d}V=\int_{\Omega}[\dot{\boldsymbol{\tau}}:\delta\mathbf{L}-(\boldsymbol{\tau}\mathbf{L}^{\mathrm{T}}):\delta\mathbf{L}]\,\mathrm{d}V. \tag{A.1}$$

Introduction of the Jaumann rate of the Kirchoff stress, $\overset{\forall}{\boldsymbol{\tau}}=\dot{\boldsymbol{\tau}}-\mathbf{W}\boldsymbol{\tau}+\boldsymbol{\tau}\mathbf{W}$ into Eq. (A.1) yields

$$\int_{\Omega}\dot{\mathbf{S}}:\operatorname{grad}\delta\mathbf{v}\,\mathrm{d}V=\int_{\Omega}\left[\overset{\forall}{\boldsymbol{\tau}}:\delta\mathbf{D}-\boldsymbol{\tau}:(\delta\mathbf{L}^{\mathrm{T}}\mathbf{L}-2\mathbf{D}\delta\mathbf{D})\right]\mathrm{d}V, \tag{A.2}$$

where $\mathbf{D}$ is the symmetric part of $\mathbf{L}$, $\mathbf{D}=(1/2)(\mathbf{L}+\mathbf{L}^{\mathrm{T}})$.

For the second term of Eq. (12) it is assumed that the magnitude of the applied tractions is fixed and the change in their intensities arises due to the change in geometry. Therefore, $\dot{\mathbf{t}}$ depends only on the deformation gradient and it can be written as

$$\dot{\mathbf{t}}=\frac{\partial\mathbf{t}}{\partial\mathbf{F}}:\dot{\mathbf{F}}=\frac{\partial\mathbf{t}}{\partial\mathbf{F}}:\mathbf{L}. \tag{A.3}$$

Assuming a hypoelastic constitutive law

$$\overset{\forall}{\boldsymbol{\tau}}=\mathbb{C}:\mathbf{D}, \tag{A.4}$$

with the fourth-order tensor $\mathbb{C}$ related to the fourth-order tensor $\mathbb{L}$ defined in Eq. (10) through

$$\mathbb{L}_{ijkl}=\mathbb{C}_{ijkl}+\tfrac{1}{2}(\sigma_{il}\delta_{jk}-\sigma_{jl}\delta_{ik}-\sigma_{jk}\delta_{il}-\sigma_{ik}\delta_{jl}), \tag{A.5}$$

Eq. (12) can be rewritten as

$$\int_{\Omega}\delta\mathbf{D}:\mathbb{C}:\mathbf{D}\,\mathrm{d}V-\int_{\Omega}(\boldsymbol{\sigma}+\lambda\,\Delta\boldsymbol{\sigma}):(\delta\mathbf{L}^{\mathrm{T}}\mathbf{L}-2\mathbf{D}\delta\mathbf{D})\,\mathrm{d}V-\int_{\partial\Omega}\left(\frac{\partial(\mathbf{t}+\lambda\,\Delta\mathbf{t})}{\partial\mathbf{F}}:\mathbf{L}\right)\delta\mathbf{v}\,\mathrm{d}S=0, \tag{A.6}$$

where $\lambda\,\Delta\mathbf{t}$ and $\lambda\,\Delta\boldsymbol{\sigma}$ are the linear perturbations tractions and stresses generated during buckling. Finite element discretization of Eq. (A.6) yields

$$(\mathbf{K}_0+\lambda\mathbf{K}_{\Delta})\widehat{\mathbf{v}}=0, \tag{A.7}$$

representing an eigenvalue problem. In Eq. (A.7) $\mathbf{K}_0$ is the initial stiffness matrix which accounts for the effect of the existing stresses $\boldsymbol{\sigma}$ and tractions $\mathbf{t}$ and $\mathbf{K}_{\Delta}$ is the differential stiffness matrix, generated by the perturbation stresses $\Delta\boldsymbol{\sigma}$ and tractions $\Delta\mathbf{t}$.

The algorithm described above together with subspace iteration method is used within the module *BUCKLE in ABAQUS to perform eigenvalue calculations.

Appendix B. Bloch wave calculation: application of boundary conditions (20) and (21) to Eq. (22)

Let us consider a primitive cell Y (as shown in Fig. 1 (center)) and choose the nodal numbering so that

$$\hat{\mathbf{v}} = [\,\hat{\mathbf{v}}_i \quad \hat{\mathbf{v}}_a \quad \hat{\mathbf{v}}_b\,]^T, \quad \hat{\mathbf{v}}_a = [\,\hat{\mathbf{v}}_{EF} \quad \hat{\mathbf{v}}_{EH} \quad \hat{\mathbf{v}}_E\,]^T, \quad \hat{\mathbf{v}}_b = [\,\hat{\mathbf{v}}_{HG} \quad \hat{\mathbf{v}}_{FG} \quad \hat{\mathbf{v}}_F \quad \hat{\mathbf{v}}_H \quad \hat{\mathbf{v}}_G\,]^T, \tag{B.1}$$

and

$$\dot{\mathbf{f}} = [\,\dot{\mathbf{f}}_i \quad \dot{\mathbf{f}}_a \quad \dot{\mathbf{f}}_b\,]^T, \quad \dot{\mathbf{f}}_a = [\,\dot{\mathbf{f}}_{EF} \quad \dot{\mathbf{f}}_{EH} \quad \dot{\mathbf{f}}_E\,]^T, \quad \dot{\mathbf{f}}_b = [\,\dot{\mathbf{f}}_{HG} \quad \dot{\mathbf{f}}_{FG} \quad \dot{\mathbf{f}}_F \quad \dot{\mathbf{f}}_H \quad \dot{\mathbf{f}}_G\,]^T, \tag{B.2}$$

with $\hat{\mathbf{v}}_i$ and $\dot{\mathbf{f}}_i$ denoting the d.o.f. of the internal nodes and the force acting on the internal nodes and the uppercase subscripts "IJ" denote points along side "IJ". Thus the full stiffness matrix can be written as

$$\mathbf{K} = \begin{bmatrix} \mathbf{K}_{ii} & \mathbf{K}_{ia} & \mathbf{K}_{ib} \\ \mathbf{K}_{ai} & \mathbf{K}_{aa} & \mathbf{K}_{ab} \\ \mathbf{K}_{bi} & \mathbf{K}_{ba} & \mathbf{K}_{bb} \end{bmatrix}. \tag{B.3}$$

As described in Section 3.3.2 two identical meshes, one for the real and the other for the imaginary quantities are used to solve the problem, yielding to the finite element formulation

$$\begin{bmatrix} \mathbf{K} & 0 \\ 0 & \mathbf{K} \end{bmatrix} \begin{bmatrix} \hat{\mathbf{v}}^{Re} \\ \hat{\mathbf{v}}^{Im} \end{bmatrix} = \begin{bmatrix} \dot{\mathbf{f}}^{Re} \\ \dot{\mathbf{f}}^{Im} \end{bmatrix}, \tag{B.4}$$

Noting from Eqs. (20) and (21) that

$$\begin{bmatrix} \hat{\mathbf{v}}_b^{Re} \\ \hat{\mathbf{v}}_b^{Im} \end{bmatrix} = \mathbf{Q}_v \begin{bmatrix} \hat{\mathbf{v}}_a^{Re} \\ \hat{\mathbf{v}}_a^{Im} \end{bmatrix} \quad \text{and} \quad \begin{bmatrix} \dot{\mathbf{f}}_b^{Re} \\ \dot{\mathbf{f}}_b^{Im} \end{bmatrix} = \mathbf{Q}_f \begin{bmatrix} \dot{\mathbf{f}}_a^{Re} \\ \dot{\mathbf{f}}_a^{Im} \end{bmatrix}, \tag{B.5}$$

($\mathbf{Q}_v$ and $\mathbf{Q}_f$ being constraint matrices containing sine and cosine factors), using the fact that $\dot{\mathbf{f}}_i = 0$ to evaluate the internal degrees of freedom $\hat{\mathbf{v}}_i$ as function of $\hat{\mathbf{v}}_a$ and multiplying both sides by $\mathbf{Q}_v^T$, Eq. (B.4) can be rewritten as

$$\tilde{\mathbf{K}} \begin{bmatrix} \hat{\mathbf{v}}_a^{Re} \\ \hat{\mathbf{v}}_a^{Im} \end{bmatrix} = 0, \tag{B.6}$$

where the matrix $\tilde{\mathbf{K}}$ is symmetric.

References

Åberg, M., Gudmundson, P., 1997. The usage of standard finite element codes for computation of dispersion relations in materials with periodic microstructure. J. Acoust. Soc. Am. 102, 2007–2013.

Aschwanden, M., Stemmer, A., 2006. Polymeric, electrically tunable diffraction grating based on artificial muscles. Opt. Lett. 31, 2610–2612.

Barthlott, W., Neinhuis, C., 1997. Purity of the sacred lotus, or escape from contamination in biological surfaces. Planta 202, 1–8.

Bertoldi, K., Boyce, M.C., 2008. Mechanically triggered transformations of phononic band gaps in periodic elastomeric structures. Phys. Rev. B 77, 052105.

Boyce, M.C., Socrate, S., Kear, K., Yeh, O., Shaw, K., 2001. Micromechanisms of deformation and recovery in thermo-plastic vulcanizates. J. Mech. Phys. Solids 49, 1323–1342.

Boyce, M.C., Prange, S.M., Bertoldi, K., Deschanel, S., Mullin, T., 2008. Mechanics of periodic elastomeric structures. In: Boukamel, Laiarinandrasana, Meo, Verron (Eds.), Constitutive Models for Rubber, vol. V. Taylor & Francis Group, London, pp. 3–7.

Campbell, M., Sharp, D.N., Harrison, M.T., Denning, R.G., Turberfield, A.J., 2000. Fabrication of photonic crystals for the visible spectrum by holographic lithography. Nature 404, 53–56.

Cheng, J.Y., Mayes, A.M., Ross, C.A., 2004. Nanostructure engineering by templated self-assembly of block copolymers. Nat. Mater. 3, 823–828.

Choi, T., Jang, J.H., Ullal, C.K., LeMieux, M.C., Tsukruk, V.V., Thomas, E.L., 2006. The elastic properties and plastic behavior of two-dimensional polymer structures fabricated by laser interference lithography. Adv. Funct. Mater. 16, 1324–1330.

Danielsson, M., Parks, D.M., Boyce, M.C., 2002. Three-dimensional micromechanical modeling of voided polymeric materials. J. Mech. Phys. Solids 50, 351–379.

Geymonat, G., Muller, S., Triantafyllidis, N., 1993. Homogenization of nonlinearly elastic materials, microscopic bifurcation and macroscopic loss of rank-one convexity. Arch. Ration. Mech. Anal. 122, 231–290.

Ghiradella, H., 1994. Structure of butterfly scales: patterning in an insect cuticle. Micros. Res. Technol. 27, 429–438.

Gibson, L.J., Ashby, M.F., 1997. Cellular Solids: Structure and Properties. Cambridge University Press.

Hennessy, K., Reese, C., Badolato, A., Wang, C.F., Imamoglu, A., Petroff, P.M., Hu, E., 2003. Fabrication of high Q square-lattice photonic crystal micro-cavities. J. Vac. Sci. Technol. B 21, 2918–2921.

Hibitt, Karlsson, Sorensen, 2006. ABAQUS Theory Manual (Version 6.6). Copyright 2006 Hibbitt, Karlsson & Sorensen, Inc.

Jang, J.H., Ullal, C.K., Tsukruk, V.V., Thomas, E.L., 2006. Mechanically tunable three dimensional elastomeric network/air structures via interference lithography. Nano Letters 6, 740–743.

Kafesaki, M., Sigalas, M.M., Economou, E.N., 1995. Elastic wave band gaps in 3-D periodic polymer matrix composites. Solid State Commun. 96, 285–289.

Kemp, D.J., Vukusic, P., Rutowski, R.L., 2006. Stress-mediated covariance between nano-structural architecture and ultraviolet butterfly coloration. Ecology 20, 282–289.

Kinoshita, S., Yoshioka, S., 2005. Structural colors in nature: the role of regularity and irregularity in the structure. Chem. Phys. Chem. 6, 1442–1459.

Kittel, C., 1986. Introduction to Solid State Physics, seventh ed. Wiley, New York, Chichester.

Kushwaha, M.S., Halevi, P., Dobrzynski, L., Djafari-Rouhani, B., 1993. Acoustic band-structure of periodic elastic composites. Phys. Rev. Lett. 71, 2022–2025.

Laroussi, M., Sab, K., Alaoui, A., 2002. Foam mechanics: nonlinear response of an elastic 3D-periodic microstructure. Int. J. Solids Struct. 39, 3599–3623.

Lee, W., Jin, M.K., Yoo, W.C., Lee, J.K., 2004. Nanostructuring of a polymeric substrate with well-defined nanometer-scale topography and tailored surface wettability. Langmuir 20, 7665–7669.

Muller, S., 1987. Homogenization of nonconvex integral functionals and cellular elastic materials. Arch. Ration. Mech. Anal. 99, 189–212.

Mullin, T., Deschanel, S., Bertoldi, K., Boyce, M.C., 2007. Pattern transformation triggered by deformation. Phys. Rev. Lett. 99, 084301.

Neinhuis, C., Barthlott, W., 1997. Characterization and distribution of water-repellent, self-cleaning plant surfaces. Ann. Bot. 79, 667–677.

Ohno, N., Okumura, D., Noguchi, H., 2002. Microscopic symmetric bifurcation condition of cellular solids based on a homogenization theory of finite deformation. J. Mech. Phys. Solids 50, 1125–1153.

Okumura, D., Ohno, N., Noguchi, H., 2004. Elastoplastic microscopic bifurcation and post-bifurcation behavior of periodic cellular solids. J. Mech. Phys. Solids 52, 641–666.

Papka, S.D., Kyriakides, S., 1994. In-plane compressive response and crushing of honeycomb. J. Mech. Phys. Solids 42, 1499–1532.

Papka, S.D., Kyriakides, S., 1998a. Experiments and full-scale numerical simulations of in-plane crushing of a honeycomb. Acta Mater. 35, 2765–2776.

Papka, S.D., Kyriakides, S., 1998b. In-plane crushing of a polycarbonate honeycomb. Int. J. Solids Struct. 35, 239–267.

Papka, S.D., Kyriakides, S., 1999a. Biaxial crushing of honeycombs—Part I: Experiments. Int. J. Solids Struct. 36, 4367–4396.

Papka, S.D., Kyriakides, S., 1999b. In-plane biaxial crushing of honeycombs—Part II: Analysis. Int. J. Solids Struct. 36, 4397–4423.

Park, W., Lee, J.B., 2004. Mechanically tunable photonic crystal structure. Appl. Phys. Lett. 85, 4845–4847.

Parker, A.R., Lawrence, C.R., 2001. Water capture by a desert beetle. Nature 414, 33–34.

Parker, A.R., McPhedran, R.C., McKenzie, D.R., Botten, L.C., Nicorovici, N.A.P., 2001. Photonic engineering—Aphrodite's Iridescence. Nature 409, 36–37.

Prange, S.M., Boyce, M.C., Bertoldi, K., Deschanel, S., Mullin, T., 2007. Mechanics of periodic elastomeric structures. In: Proceedings of the 5th European Conference on Constitutive Models for Rubber, ECCMR 2007, Paris, France.

Prum, R.O., Quinn, T., Torres, R.H., 2006. Anatomically diverse butterfly scales all produce structural colours by coherent scattering. J. Exp. Biol. 209, 748–765.

Rivlin, R.S., Saunders, D.W., 1951. Large elastic deformations of isotropic materials, VII, experiments on the deformation of rubber. Trans. R. Soc. Lond., Ser. A 243, 251–288.

Saiki, I., Terada, K., Ikeda, K., Hori, M., 2002. Appropriate number of unit cells in a representative volume element for micro-structural bifurcation encountered in multi-scale modeling. Comput. Meth. Appl. Mech. Eng. 191, 2561–2585.

Shevchenko, E.V., Talapin, D.V., Kotov, N.A., O'Brien, S., Murray, C.B., 2006. Structural diversity in binary nanoparticle superlattices. Nature 439, 55–59.

Tantikom, K., Aizawa, T., Mukai, T., 2005a. Symmetric and asymmetric deformation transition in the regularly cell-structured materials. Part II: Theoretical study. Int. J. Solids Struct. 42, 2211–2224.

Tantikom, K., Aizawa, T., Mukai, T., 2005b. Symmetric and asymmetric deformation transition in the regularly cell-structured materials. Part I: experimental study. Int. J. Solids Struct. 42, 2199–2210.

Thylen, L., Qiu, M., Anand, S., 2004. Photonic crystals—a step towards integrated circuits for photonics. Chem. Phys. Chem. 5, 1268–1283.

Triantafyllidis, N., Schnaidt, W.C., 1993. Comparison of microscopic and macroscopic instabilities in a class of two-dimensional periodic composites. J. Mech. Phys. Solids 41, 1533–1565.

Triantafyllidis, N., Schraad, M.W., 1998. Onset of failure in aluminum honeycombs under general in-plane loading. J. Mech. Phys. Solids 46, 1089–1124.

Triantafyllidis, N., Nestorovic, M.D., Schraad, M.W., 2006. Failure surfaces for finitely strained two-phased periodic solids under general in-plane loading. J. Appl. Mech. 73, 505–515.

Ullal, C.K., Maldovan, M., Thomas, E.L., Chen, G., Han, Y.J., Yang, S., 2004. Photonic crystals through holographic lithography: simple cubic, diamond-like, and gyroid-like structures. Appl. Phys. Lett. 84, 5434–5436.

Vukusic, P., Sambles, J.R., 2003. Photonic structures in biology. Nature 424, 852–855.

Wagner, T., Neinhuis, C., Barthlott, W., 1996. Wettability and contaminability of insect wings as a function of their surface sculpture. Acta Zool. 77, 213–225.

Yang, S.X., Page, J.H., Liu, Z.Y., Cowan, M.L., Chan, C.T., Sheng, P., 2004. Focusing of sound in a 3D phononic crystal. Phys. Rev. Lett. 93, 024301.

Zhai, L., Berg, M.C., Cebeci, F.C., Kim, Y., Milwid, J.M., Rubner, M.F., Cohen, R.E., 2006. Patterned super-hydrophobic surfaces: toward a synthetic mimic of the Namib Desert beetle. Nano Letters 6, 1213–1217.

Zuriguel, I., Mullin, T., Rotter, J.M., 2007. The effect of particle shape on the stress dip under a sandpile. Phys. Rev. Lett. 98, 028001.